RESEARCH ARTICLE

Mesenchymal Lineage Heterogeneity Underlies Nonredundant Functions of Pancreatic Cancer–Associated Fibroblasts

Erin J. Helms[1], Mark W. Berry[1], R. Crystal Chaw[2], Christopher C. DuFort[3], Duanchen Sun[4], M. Kathrina Onate[1], Chet Oon[1], Sohinee Bhattacharyya[1], Hannah Sanford-Crane[1], Wesley Horton[1], Jennifer M. Finan[1], Ariana Sattler[1], Rosemary Makar[5], David W. Dawson[6], Zheng Xia[4], Sunil R. Hingorani[3,7,8], and Mara H. Sherman[1,9]

Illustration by Bianca Dunn

ABSTRACT Cancer-associated fibroblast (CAF) heterogeneity is increasingly appreciated, but the origins and functions of distinct CAF subtypes remain poorly understood. The abundant and transcriptionally diverse CAF population in pancreatic ductal adenocarcinoma (PDAC) is thought to arise from a common cell of origin, pancreatic stellate cells (PSC), with diversification resulting from cytokine and growth factor gradients within the tumor microenvironment. Here we analyzed the differentiation and function of PSCs during tumor progression *in vivo*. Contrary to expectations, we found that PSCs give rise to a numerically minor subset of PDAC CAFs. Targeted ablation of PSC-derived CAFs within their host tissue revealed nonredundant functions for this defined CAF population in shaping the PDAC microenvironment, including production of specific extracellular matrix components and tissue stiffness regulation. Together, these findings link stromal evolution from distinct cells of origin to transcriptional heterogeneity among PDAC CAFs and demonstrate unique functions for CAFs of a defined cellular origin.

SIGNIFICANCE: By tracking and ablating a specific CAF population, we find that a numerically minor CAF subtype from a defined cell of origin plays unique roles in establishing the pancreatic tumor microenvironment. Together with prior studies, this work suggests that mesenchymal lineage heterogeneity and signaling gradients diversify PDAC CAFs.

See related commentary by Cukierman, p. 296.

INTRODUCTION

Pancreatic ductal adenocarcinoma (PDAC) is defined in part by an exuberant stromal reaction, including abundant cancer-associated fibroblasts (CAF; refs. 1–4). Diverse tumor-supportive functions have been ascribed to PDAC CAFs, including metabolic roles whereby nutrient transfer from CAFs to neighboring pancreatic cancer cells facilitates proliferation within a nutrient-poor microenvironment (5–9). In addition, PDAC CAFs produce cytokines and chemokines associated with immune suppression (10–13), and CAF ablation in mice fosters efficacy of immune checkpoint inhibitors that are otherwise ineffective in PDAC (14, 15). Furthermore, perhaps the best-known function of activated fibroblasts in a wound-healing reaction and of CAFs in a tumor microenvironment is to produce extracellular matrix (ECM) components and remodeling enzymes. The dense ECM in PDAC physically impedes the vasculature and limits delivery of intravenous therapeutic agents (16, 17), and patients with PDAC who have high levels of stiff fibrosis enriched for matricellular proteins (such as tenascin C; TNC) have shortened survival (18). These findings have motivated efforts to develop therapies targeting CAFs, including inhibitors of pathways that regulate their phenotypes (e.g., the Hedgehog pathway; refs. 19, 20) or their immunomodulatory functions (e.g., the CXCL12–CXCR4 axis; refs. 14, 21) and agents targeting the ECM itself (22).

However, the impact of CAFs on PDAC progression and the therapeutic potential of targeting these cells are controversial. Genetic or pharmacologic ablation of CAFs during PDAC progression in mice—either by targeting α-smooth muscle actin (α-SMA)–expressing CAFs (15) or Sonic Hedgehog (SHH)–dependent CAFs (23, 24)—resulted in poorly differentiated tumors and caused faster demise than animals with CAF-replete PDAC. Stromal depletion of ECM component type I collagen significantly accelerated mortality in PDAC-bearing mice (25), and inhibition of collagen cross-linking by LOXL2 increased PDAC growth and reduced overall survival (26). Similarly, higher tumor stromal density, including cellular and acellular components of the stroma, associated with longer overall survival among patients with PDAC (26, 27). These studies highlight the tumor-suppressive or homeostatic potential of PDAC CAFs and impel a more thorough understanding of this complex compartment of the tumor microenvironment with respect to disease progression.

[1]Department of Cell, Developmental & Cancer Biology, Oregon Health & Science University, Portland, Oregon. [2]Advanced Light Microscopy Shared Resource, Oregon Health & Science University, Portland, Oregon. [3]Clinical Research Division, Fred Hutchinson Cancer Research Center, Seattle, Washington. [4]Department of Computational Biology, Oregon Health & Science University, Portland, Oregon. [5]Knight BioLibrary, Oregon Health & Science University, Portland, Oregon. [6]Department of Pathology and Laboratory Medicine and Jonsson Comprehensive Cancer Center, David Geffen School of Medicine at the University of California, Los Angeles, Los Angeles, California. [7]Public Health Sciences Division, Fred Hutchinson Cancer Research Center, Seattle, Washington. [8]Division of Medical Oncology, University of Washington School of Medicine, Seattle, Washington. [9]Knight Cancer Institute, Oregon Health & Science University, Portland, Oregon.

Corresponding Author: Mara H. Sherman, Department of Cell, Developmental & Cancer Biology, Oregon Health & Science University, 2730 S. Moody Avenue CL6C, Portland, OR 97201. Phone: 503-346-9012; E-mail: shermama@ohsu.edu

Cancer Discov 2022;12:484–501

doi: 10.1158/2159-8290.CD-21-0601

To reconcile these seemingly contradictory findings, several groups have postulated that PDAC CAFs are heterogeneous, potentially including subtypes that both support and suppress tumor growth. Consistent with this notion, single-cell RNA sequencing (RNA-seq) and other approaches have revealed transcriptional heterogeneity among CAFs in murine and human PDAC (11, 12, 28–30). Key considerations moving forward are the origins of these CAF subtypes and, importantly, their functions. Understanding the potentially unique functions of CAF subtypes is needed for identifying and specifically targeting the tumor-promoting mechanisms in the stroma. Understanding CAF cellular origin(s) is important because blocking the development or activation of tumor-supportive CAF subtypes may be a viable therapeutic strategy. Identifying CAF origin is also important for the goal of developing new models to track and manipulate CAFs within their host tissue in a robust and specific way, as such models are presently lacking.

PDAC CAFs are generally thought to share a common cell of origin: a tissue-resident mesenchymal cell called a stellate cell (31, 32). Stellate cells are found in two tissues in the body, the liver and the pancreas (33), and were previously called Ito cells or lipocytes (34). Cre-based models have informed on hepatic stellate cell (HSC) fate and function (35, 36), but these models have not been used successfully to study pancreatic stellate cells (PSC). As a result, our understanding of PSC biology to date has been extrapolated from the liver or from cell culture studies.

In healthy pancreas tissue, PSCs are in a quiescent state, characterized in part by cytoplasmic lipid droplets that store vitamin A as retinyl esters and implicated in tissue homeostasis, including recycling of the basement membrane (37), although our understanding of normal PSC function is limited due to the lack of specific models. Upon exposure to tissue damage cues or a stiff growth substrate, PSCs become activated to a myofibroblastic phenotype. As PSCs can be isolated from healthy pancreata by density centrifugation on the basis of their lipid content, PSC activation can be modeled *in vitro*. Transcriptional profiling of PSC activation showed upregulation of ECM components and remodeling enzymes, growth factors, and other signatures associated with CAFs, suggesting that PSCs are indeed competent to give rise to CAFs during PDAC progression. However, as these cells have not been tracked *in vivo* in the context of tumorigenesis, their contribution to the PDAC microenvironment and their functions therein remain unknown. Recent work demonstrated that PDAC CAF heterogeneity results in part from signaling gradients of critical factors, including TGFβ and IL1 (12, 38), and that these factors can differentially program PSCs into inflammatory or myofibroblastic CAF (myCAF) fates *in vitro*. To analyze the fate of PSCs in PDAC *in vivo*, we developed a mouse model in which we can track and specifically ablate these cells within the pancreas, leveraging their unique lipid-storing origin. We find that PSCs indeed give rise to CAFs but that this PSC-derived CAF population is numerically minor, suggesting additional and yet undefined cellular origins for most PDAC CAFs. Importantly, PSC-derived CAFs play significant, nonredundant roles in modulation of the tumor microenvironment, including production of specific components of the ECM, suggesting that these cells or their critical regulators may be therapeutic targets.

RESULTS

Characterization of a Genetic Approach to Label and Track Stellate Cells in Normal Pancreas Tissue

To identify a Cre-based approach to label and track PSCs *in vivo*, we analyzed published RNA-seq data from primary PSCs and noted very high expression of the adipocyte marker fatty acid binding protein 4 (Fabp4) in the quiescent state (39). Although Fabp4 expression was dramatically downregulated in the activated, fibroblastic state, we reasoned that a lineage-labeling approach driven by Fabp4 regulatory elements would label PSCs as well as CAFs derived from them. To address the utility of this approach, we crossed *Fabp4-Cre* mice, developed to study adipose tissue (40), to mice harboring the *Rosa26*$^{\text{ACTB-tdTomato,-EGFP}}$ (*Rosa26*$^{\text{mTmG}}$ hereafter) reporter allele (ref. 41; Fig. 1A). In these mice, the ubiquitous *Rosa26* promoter drives expression of tdTomato followed by a stop codon; in the presence of Cre, tdTomato and the stop codon are excised, leading to expression of GFP. As such, all cells of the mouse express tdTomato except Cre-positive cells and their progeny, which are indelibly labeled with GFP. When we examined pancreata of *Fabp4-Cre;Rosa*$^{\text{mTmG}}$ mice, we noted rare GFP$^+$ cells in the periacinar spaces of the expected morphology and frequency for PSCs based on previously published PSC characterization and electron microscopy analyses (refs. 42, 43; Fig. 1B). We characterized these GFP$^+$ cells in the pancreas to assess whether this lineage label was specific to PSCs within normal pancreas tissue and whether GFP labeling was pervasive among PSCs. To assess specificity, we analyzed GFP together with markers of other known pancreatic cell types, as strong markers for PSCs are largely lacking. We

Figure 1. Fabp4-Cre marks stellate cells specifically and pervasively within normal pancreas tissue. **A,** Schematic of the alleles used to label and track PSCs *in vivo*. **B,** Representative image of normal pancreas tissue from *Fabp4-Cre;Rosa26*$^{\text{mTmG}}$ mice ($n = 7$) showing rare GFP$^+$ cells within a predominantly tdTomato$^+$ tissue. Scale bar, 50 μm. **C,** Representative image of normal pancreas tissue from *Fabp4-Cre;Rosa26*$^{\text{mTmG}}$ mice ($n = 3$) showing CD31$^+$ endothelial cells and GFP$^+$ cells, some of which are adjacent to vessels. Top images: scale bar, 50 μm; bottom images: scale bar, 10 μm. **D,** Representative image of normal pancreas tissue from *Fabp4-Cre;Rosa26*$^{\text{mTmG}}$ mice ($n = 3$) showing CD45$^+$ leukocytes and GFP$^+$ cells. Scale bar, 10 μm. **E,** Representative image of normal pancreas tissue from *Fabp4-Cre;Rosa26*$^{\text{mTmG}}$ mice ($n = 3$) showing NG2$^+$ pericytes and GFP$^+$ cells. Scale bar, 50 μm. **F,** qPCR for the indicated genes in GFP$^+$ and tdTomato$^+$ cells isolated from normal pancreas tissue from *Fabp4-Cre;Rosa26*$^{\text{mTmG}}$ mice by FACS ($n = 3$, with each replicate pooled from two mice), including markers of pericytes (*Cspg4*; liver is a positive control), stellate cells and potentially other mesenchymal cells (*Des*), ductal cells (*Krt19*), mesenchymal cells (*Vim*), acinar cells (*Prss3*), and β cells (*Ins1*); *Fabp4* was included as a control. Data were normalized to *36b4* and are presented as mean ± SEM. **G,** Quantification of GFP$^+$ cells and tdTomato$^+$ cells out of total, desmin$^+$ PSCs isolated by density centrifugation from normal pancreas tissue in *Fabp4-Cre;Rosa26*$^{\text{mTmG}}$ mice ($n = 3$) and analyzed by immunofluorescence microscopy. Data are presented as mean ± SEM. **H,** Flow cytometry results depicting GFP$^+$ and tdTomato$^+$ cells among all vitamin A$^+$ PSCs in normal pancreas tissue from *Fabp4-Cre;Rosa26*$^{\text{mTmG}}$ mice ($n = 3$). Data are presented as mean ± SEM.

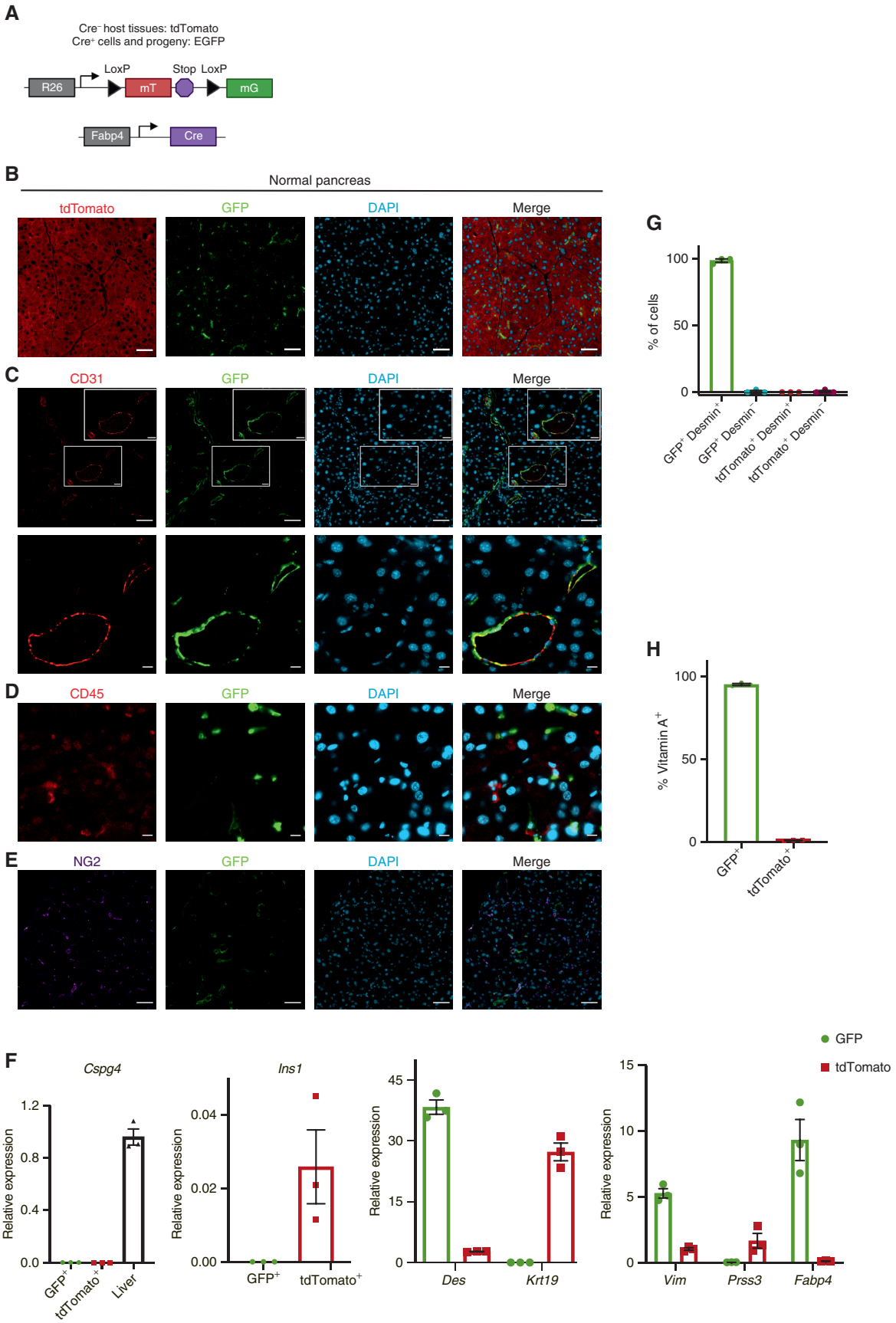
A
Cre⁻ host tissues: tdTomato
Cre⁺ cells and progeny: EGFP
R26
LoxP
mT
Stop
LoxP
mG
Fabp4
Cre
B
Normal pancreas
tdTomato
GFP
DAPI
Merge
C
CD31
GFP
DAPI
Merge
D
CD45
GFP
DAPI
Merge
E
NG2
GFP
DAPI
Merge
G
% of cells
100
50
0
GFP⁺ Desmin⁺
GFP⁺ Desmin⁻
tdTomato⁺ Desmin⁺
tdTomato⁺ Desmin⁻
H
% Vitamin A⁺
100
50
0
GFP⁺
tdTomato⁺
F
Cspg4
Ins1
Des
Krt19
Vim
Prss3
Fabp4
Relative expression
GFP
tdTomato
GFP⁺
tdTomato⁺
Liver

found that CD31$^+$ endothelial cells, CD45$^+$ leukocytes, and NG2$^+$ pericytes were restricted to the tdTomato$^+$ population and lacked the GFP lineage label (Fig. 1C–E; Supplementary Fig. S1A). Although CD31$^+$ endothelial cells were all tdTomato$^+$, we did note the perivascular localization of a subset of PSCs, as has been reported for HSCs (Fig. 1C; ref. 35). To further address specificity, we isolated tdTomato$^+$ and GFP$^+$ cells from the pancreas by FACS (Supplementary Fig. S1B) and measured expression of markers for pancreatic cell types by qPCR (Fig. 1F). We did not see an enrichment for *Cspg4* (which encodes the pericyte marker NG2) in the GFP$^+$ fraction, suggesting that the numerically small pericyte population is within the far more numerous tdTomato$^+$ cell population (liver was a positive control). Markers of acinar cells, ductal cells, and β cells were restricted to the tdTomato$^+$ fraction, whereas mesenchymal marker *Vim* and putative stellate cell/mesenchymal marker *Des* were strongly enriched in the GFP$^+$ fraction. These results suggest that GFP specifically marks PSCs within the pancreas of *Fabp4-Cre;Rosa26*^{mTmG} mice.

We next assessed whether GFP pervasively marks PSCs in *Fabp4-Cre;Rosa26*^{mTmG} mice, which we analyzed in two ways. We isolated PSCs from the pancreas by density centrifugation, which broadly captures quiescent PSCs on the basis of their lipid content. As this is an enrichment, not a purification, we plated cells at the interface and stained for desmin to increase confidence that our analysis extended to all PSCs but not to any contaminating cell types of similar density. We found that nearly all PSCs identified by this approach were GFP$^+$ (Fig. 1G; Supplementary Fig. S1C). To analyze this a second way, we took advantage of perhaps the best-known function of quiescent stellate cells, namely, storage of vitamin A in their cytoplasmic lipid droplets as retinyl esters. This retinoid storage gives stellate cells a blue–green autofluorescence that can be analyzed by flow cytometry, as previously demonstrated for HSCs (44). Flow cytometric analysis revealed the expected frequency of vitamin A$^+$ PSCs in a single-cell suspension of normal pancreas from *Fabp4-Cre;Rosa26*^{mTmG} mice (Supplementary Fig. S1D). Moreover, we found that nearly all of these vitamin A$^+$ PSCs were GFP$^+$ (Fig. 1H). These results together suggest that *Fabp4-Cre;Rosa26*^{mTmG} mice feature specific and pervasive GFP labeling of stellate cells within the pancreas.

Analysis of Stellate Cell Contribution to the CAF Pool in the PDAC Microenvironment

As our model allows us to track the fate of PSCs during pancreatic tumorigenesis, we used *Fabp4-Cre;Rosa26*^{mTmG} mice to formally address the contribution of PSCs to the PDAC CAF population. Upon transplantation of *Kras*$^{LSL\text{-}G12D/+}$*; Trp53*$^{LSL\text{-}R172H/+}$*;Pdx1-Cre* (KPC; ref. 45) PDAC cells into the pancreas of *Fabp4-Cre;Rosa26*^{mTmG} hosts, we consistently observed an expansion of GFP$^+$ cells in the tumor microenvironment with a CAF-like morphology (Fig. 2A). To characterize these GFP$^+$ stromal cells, we stained for CAF markers including the pan-CAF marker Podoplanin (PDPN; ref. 11) and the myCAF marker α-SMA (28). We found that GFP$^+$ or PSC-derived CAFs expressed these markers (Fig. 2B and C), confirming that PSCs give rise to PDAC CAFs and demonstrating that they yield a subset of CAFs within the previously established myCAF subpopulation. Although we acknowledge the limitations of transplantation models, we note that total PDPN-positive cells across our models are similar in frequency to that reported in autochthonous PDAC (ref. 12; Fig. 2D). Contrary to our expectations, however, we noted across PDAC models that PSCs give rise to only a small minority of CAFs, raising the possibility that previously described transcriptional heterogeneity among these cells is due in part to distinct cells of origin. We confirmed these findings by flow cytometry, which showed that, in two different KPC-derived models and using two different CAF cell-surface markers (PDPN or PDGFRα), PSC-derived CAFs give rise to approximately 10% to 15% of total PDPN$^+$ CAFs (Fig. 2E–G). These results indicate that PSCs give rise to a numerically minor subset of PDAC CAFs and prompted us to examine whether this PSC-derived CAF population plays unique roles in the tumor microenvironment or whether these CAFs harbor similar transcriptional profiles and functions to CAFs of other cellular origins.

Distinct Transcriptional Profiles of CAFs from a Stellate Cell or Non–Stellate Cell Origin

To assess the potential nonredundancy of PSC-derived CAFs, we analyzed their transcriptional profiles. To this end, we established PDAC in *Fabp4-Cre;Rosa26*^{mTmG} hosts, isolated GFP$^+$ (PSC-derived) and tdTomato$^+$ (non–PSC-derived) CAFs by FACS, and performed RNA-seq (Supplementary Table S1). This analysis revealed that both CAF populations express similar levels of broad or pan-CAF markers, including *Fap* (which encodes fibroblast activation protein) and *Pdpn*, and that both populations express very high levels of *Acta2* (which encodes α-SMA), *Lrrc15* (12), and similar levels of the majority of collagen genes. However, we found extensive transcriptional differences between these CAF populations (Fig. 3A and B), suggesting that transcriptional heterogeneity among PDAC CAFs is influenced not only by cytokine and growth factor gradients within the tumor microenvironment but also by mesenchymal lineage ($\log_2$ fold change >1, upregulated in tdTomato$^+$: 1,163 genes; $\log_2$ fold change <–1, upregulated in GFP$^+$: 427 genes). Gene ontology analysis revealed enrichment of genes in the PSC-derived CAF population involved in cell adhesion, ECM–receptor interaction,

Figure 2. Stellate cells give rise to a numerically minor subset of PDAC CAFs. **A,** IHC staining of PDAC (KPC 4662) in *Fabp4-Cre;Rosa26*^{mTmG} hosts ($n = 5$), with GFP in green and panCK (tumor cells) in red. Scale bar, 20 μm. **B,** IHC staining of PDAC (KPC FC1199) in *Fabp4-Cre;Rosa26*^{mTmG} hosts ($n = 3$), stained for GFP, PDPN, and α-SMA. Scale bar, 10 μm. **C,** IHC staining of PDAC (KP$^{flox/+}$C HY2910) in *Fabp4-Cre;Rosa26*^{mTmG} hosts ($n = 3$), stained for GFP, PDPN, and α-SMA. Scale bar, 10 μm. **D,** Quantification of IHC staining for PDPN in the indicated transplantable PDAC models. **E,** Flow cytometry analysis of PDGFRα, GFP, and tdTomato in KPC 4662 tumors in *Fabp4-Cre;Rosa26*^{mTmG} hosts ($n = 5$). Data are presented as mean ± SEM. For **E**–**G**, CAF frequency calculations excluded the tdTomato$^-$GFP$^-$ fraction constituting transplanted PDAC cells. **F,** Flow cytometry analysis of PDPN, GFP, and tdTomato in KPC FC1199 tumors in *Fabp4-Cre;Rosa26*^{mTmG} hosts ($n = 8$). Data are presented as mean ± SEM. **G,** Flow cytometry analysis of PDPN, GFP, and tdTomato in KPC 4662 tumors in *Fabp4-Cre;Rosa26*^{mTmG} hosts ($n = 3$). Data are presented as mean ± SEM.

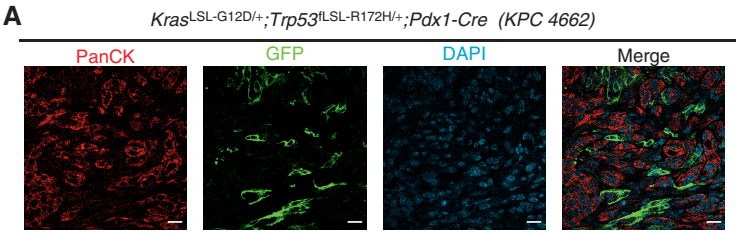
A
Kras LSL-G12D/+;Trp53 fLSL-R172H/+;Pdx1-Cre (KPC 4662)
PanCK
GFP
DAPI
Merge

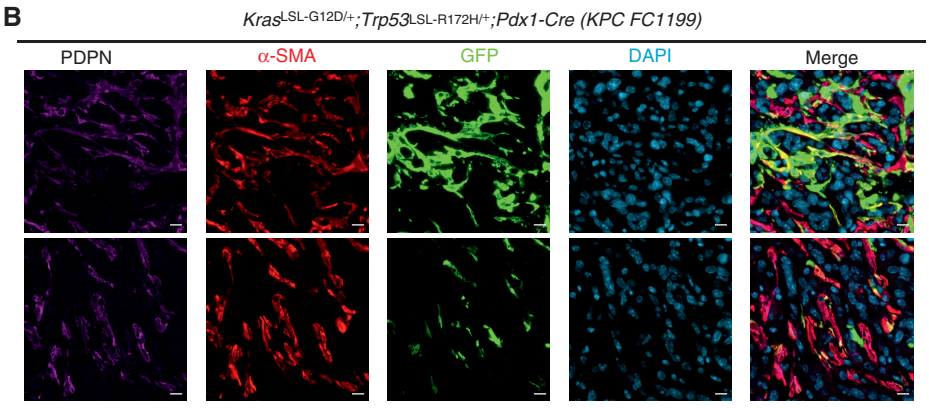
B
Kras LSL-G12D/+;Trp53 LSL-R172H/+;Pdx1-Cre (KPC FC1199)
PDPN
α-SMA
GFP
DAPI
Merge

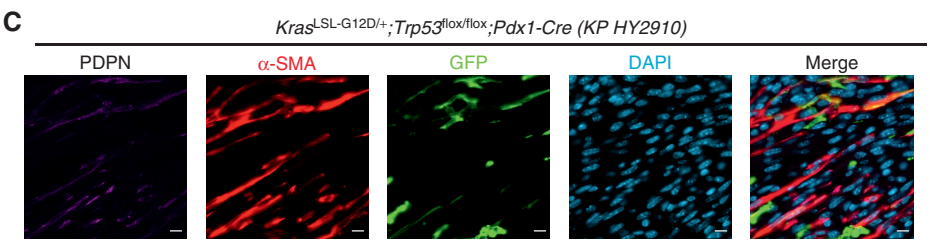
C
Kras LSL-G12D/+;Trp53 flox/flox;Pdx1-Cre (KP HY2910)
PDPN
α-SMA
GFP
DAPI
Merge

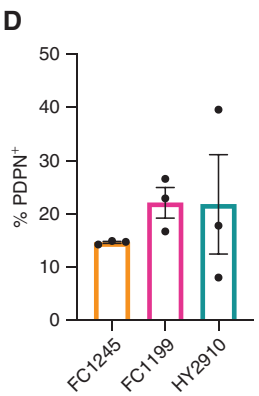
D
% PDPN+
50
40
30
20
10
0
FC1245
FC1199
HY2910

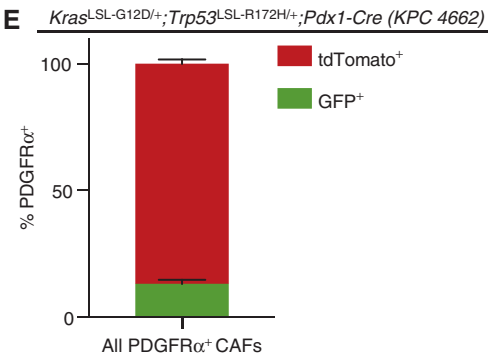
E
Kras LSL-G12D/+;Trp53 LSL-R172H/+;Pdx1-Cre (KPC 4662)
tdTomato+
GFP+
% PDGFRα+
100
50
0
All PDGFRα+ CAFs

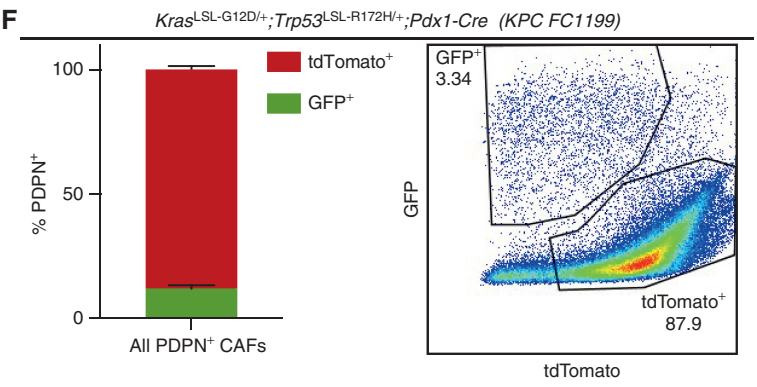
F
Kras LSL-G12D/+;Trp53 LSL-R172H/+;Pdx1-Cre (KPC FC1199)
tdTomato+
GFP+
% PDPN+
100
50
0
All PDPN+ CAFs
GFP+
3.34
GFP
tdTomato+
87.9
tdTomato

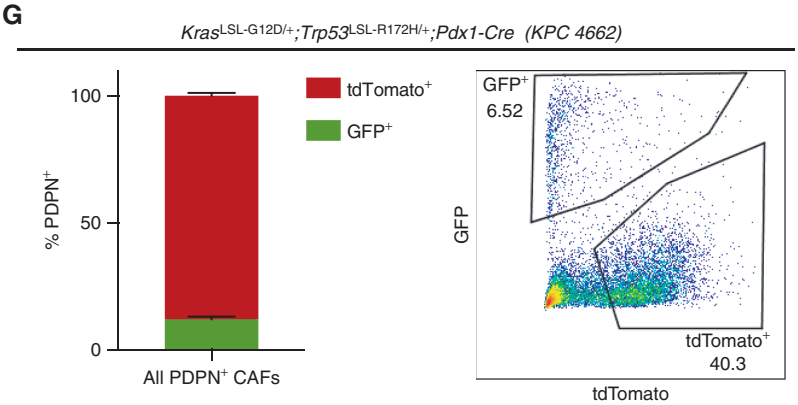
G
Kras LSL-G12D/+;Trp53 LSL-R172H/+;Pdx1-Cre (KPC 4662)
tdTomato+
GFP+
% PDPN+
100
50
0
All PDPN+ CAFs
GFP+
6.52
GFP
tdTomato+
40.3
tdTomato

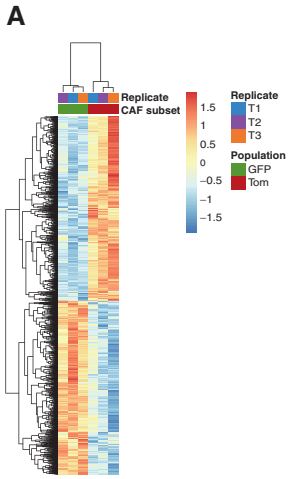

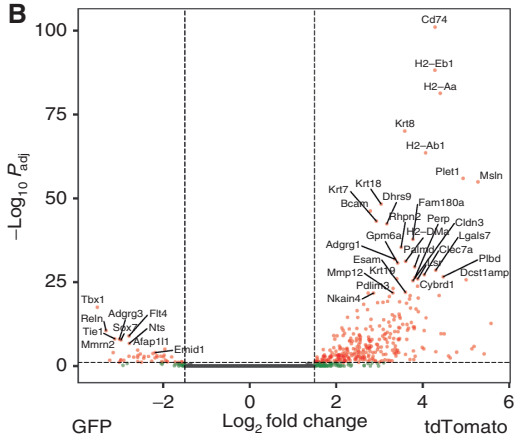

C

Term	*P* value
Cell adhesion	7.3×10^{-20}
Angiogenesis	2.3×10^{-11}
Axon guidance	1.1×10^{-8}
Multicellular organism development	5.8×10^{-7}
Negative regulation of cell migration	7.6×10^{-7}
Extracellular matrix organization	1.6×10^{-6}

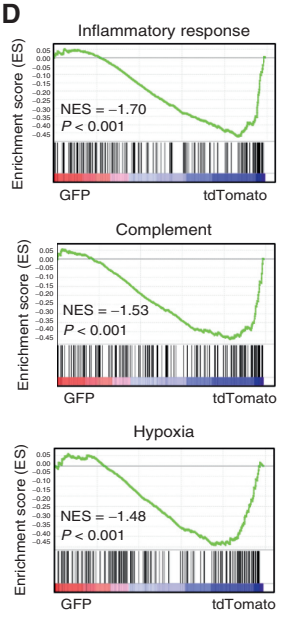

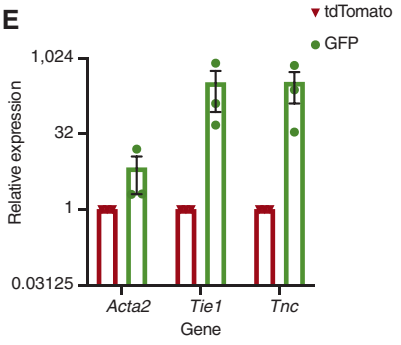

Wilcoxon rank-sum test *P* value:
myCAF vs. iCAF: 3.11×10^{-56}
myCAF vs. apCAF: 0
iCAF vs. apCAF: 1.3×10^{-297}

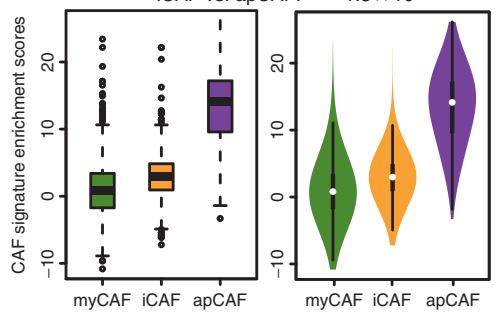

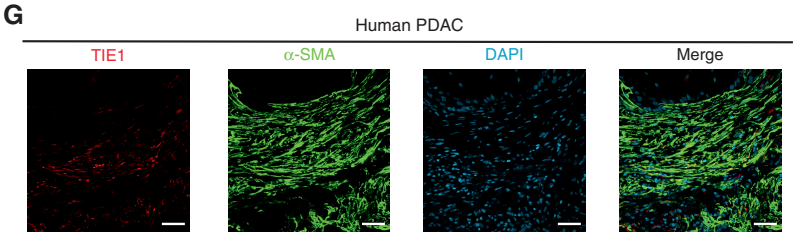

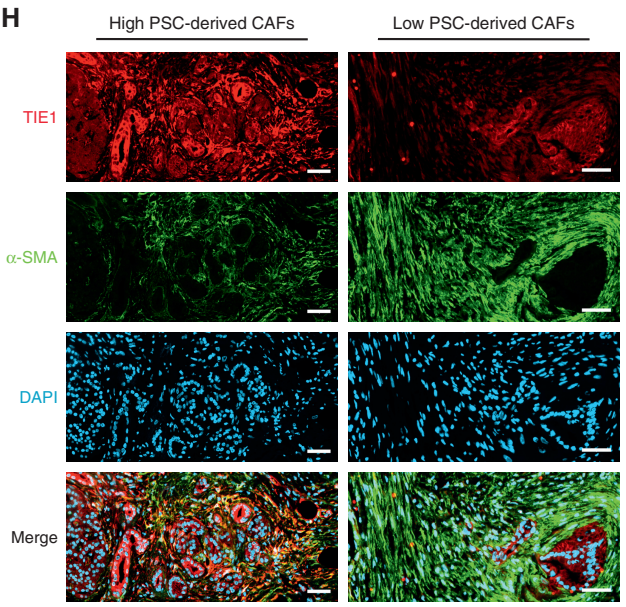

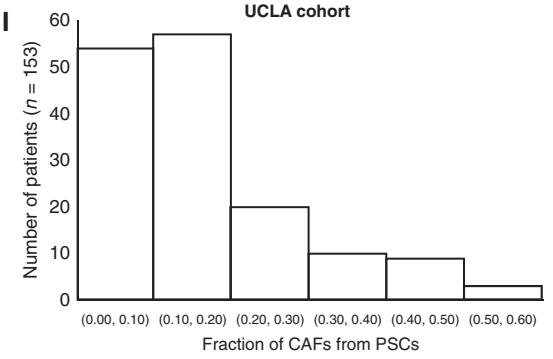

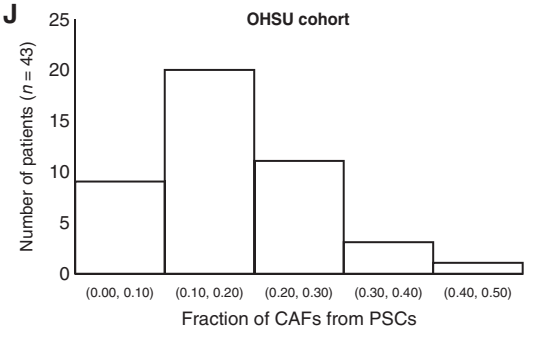

and axon guidance (Fig. 3C). Gene set enrichment analysis revealed that genes more highly expressed in CAFs of a non-PSC origin are significantly enriched for immunomodulatory processes, including "inflammatory response" and "complement" as well as metabolic processes, including "hypoxia" (Fig. 3D). The gene identities enriched among PSC-derived CAFs included cell-surface adhesion molecules that facilitate leukocyte trafficking and/or cancer cell spatial patterning but not previously characterized on CAFs, including the receptor tyrosine kinase *Tie1* (Fig. 3E; notably, *Tek* encoding TIE2 was not enriched among PSC-derived CAFs). ECM components more highly or uniquely expressed among PSC-derived CAFs include those implicated in tissue stiffness and PDAC aggressiveness, such as tenascins including *Tnc* (Fig. 3E; ref. 18) and *Hspg2*, encoding perlecan. Differential expression of *Hspg2* gains significance in light of a recent study comparing CAFs from genetically engineered mouse models of PDACs featuring mutant KRAS as well as mutant p53 (R172H) or p53 loss (46). The authors found that CAFs associated with p53-mutant PDAC are significantly more prometastatic and more effectively promote chemoresistance than CAFs from p53-null tumors, with both phenotypes driven by stromal expression of perlecan. In addition, the axon guidance cues expressed by PSC-derived CAFs include members of the Slit/Robo family, with potential implications for regulation of tumor innervation. We note that immunomodulatory cytokines and chemokines as well as genes that make up MHC class II are strongly enriched in the tdTomato$^+$ CAF fraction, suggesting that the previously described inflammatory CAFs (iCAF; ref. 28) and antigen-presenting CAFs (apCAF; ref. 11) do not have a PSC origin. This conclusion is supported by comparison of all differentially expressed genes from our RNA-seq dataset to single-cell RNA-seq data from KPC mice, which revealed that genes differentially expressed in PSC-derived versus non–PSC-derived CAFs are significantly enriched in iCAFs and apCAFs compared with myCAFs (Fig. 3F; see Supplementary Methods). Receptors for secreted factors implicated in myCAF and iCAF specification are expressed at similar levels in these CAF populations, including receptors for Hedgehog ligands, TGFβ, and IL1 (Supplementary Fig. S2A), such that downstream signaling components or the epigenetic state of PSCs may promote a myCAF transcriptional state.

We used our RNA-seq datasets to determine a marker combination for PSC-derived CAFs that could be used to analyze the frequency of this CAF population among PDAC patient samples, in order to validate the findings from our mouse models. We selected the marker combination of α-SMA, a marker of most CAFs and those in the myCAF population, which include PSC-derived CAFs, and TIE1, which is highly expressed on endothelial cells but was unique to PSC-derived CAFs among total CAFs (Supplementary Fig. S2B and S2C). In an initial cohort of PDAC patient tumor sections, we noted a minor population of TIE1$^+$α-SMA$^+$ CAFs out of the expansive α-SMA$^+$ population (Fig. 3G), consistent with patterns in our mouse models. To more extensively analyze the frequency of PSC-derived CAFs in human PDAC, including heterogeneity across a patient population, we obtained a PDAC tumor microarray containing four spatially distinct punches from each of 153 patient samples. We costained the array for TIE1 and α-SMA and quantified the double-positive CAFs out of total α-SMA$^+$ CAFs. We saw evidence of heterogeneity across this patient population, with some samples harboring relatively high levels of putative PSC-derived CAFs and others very low levels (Fig. 3H). Quantification of CAF frequencies yielded two important conclusions (Fig. 3I): First, most patient samples harbored putative PSC-derived CAFs at similar frequencies to those observed in our mouse models and, second, almost all of these patient samples had putative PSC-derived CAFs as the minority of CAFs in the tumor microenvironment, highlighting the extent of mesenchymal lineage heterogeneity. We further validated these findings in yet another independent patient cohort, costaining 43 PDAC tumor sections, here analyzing a lower "*n*" but whole sections instead of small punches on an array. We found similar results, including heterogeneity in putative PSC-derived CAF frequencies (Supplementary Fig. S2D), similar frequencies to those observed in mouse models in most patient samples (Fig. 3J), and a minority of CAFs of a presumed PSC origin in all of these patient samples. Together, these results suggest that mesenchymal lineage heterogeneity underlies transcriptional heterogeneity among PDAC CAFs and that this lineage heterogeneity is relevant to human PDAC.

Targeted Ablation of PSC-Derived CAFs via Retrograde Ductal Injection of Viral Cre to Unveil Functional Significance

We next wished to functionally interrogate PSC-derived CAFs to address whether their unique transcriptional profile translates to nonredundant roles in PDAC. To address this question, we aimed to ablate PSC-derived CAFs in established

Figure 3. Mesenchymal lineage heterogeneity gives rise to transcriptional heterogeneity among PDAC CAFs. Heat map (**A**) and volcano plot (**B**) depicting differentially expressed genes in PSC-derived (GFP$^+$) versus non–PSC-derived (tdTomato$^+$) CAFs from KPC FC1199 PDAC in *Fabp4-Cre;Rosa26*^{mTmG} hosts ($n = 3$), identified by RNA-seq. In **B**, gray circles indicate genes not different between the populations, green circles indicate genes with $\log_2$ fold change >1 or <−1, and pink circles indicate genes with the same $\log_2$ fold change criteria and $P < 0.05$. **C,** Gene ontology analysis identifying the top terms enriched in association with genes upregulated at least twofold in PSC-derived CAFs compared with non–PSC-derived CAFs. **D,** Gene set enrichment analysis showing pathways or processes with transcriptional signatures enriched in the tdTomato$^+$ CAF population. NES, normalized enrichment score. **E,** qPCR for the indicated genes on PSC-derived and non–PSC-derived CAFs sorted from KPC FC1199 PDAC in *Fabp4-Cre;Rosa26*^{mTmG} hosts ($n = 3$) by FACS. Data were normalized to *36b4* and are presented as mean ± SEM. **F,** Box (left) and violin (right) plots indicating enrichment scores for differentially expressed genes between GFP$^+$ and tdTomato$^+$ CAFs among myCAF-, iCAF-, and apCAF-associated genes per previously published small conditional RNA-seq results. **G,** Representative IHC staining of human PDAC for TIE1 and α-SMA ($n = 5$). Scale bar, 50 μm. **H,** Representative images from a human PDAC microarray after IHC staining for TIE1 and α-SMA ($n = 153$). Scale bar, 50 μm. **I,** Quantification of TIE1$^+$α-SMA$^+$ area out of total α-SMA$^+$ area on each patient sample from the array. Different regions from the same patient were averaged together to yield one frequency per patient sample (four punches per patient, 612 total tumor regions analyzed, 153 plotted here after averaging for each patient). **J,** Quantification of TIE1$^+$α-SMA$^+$ area out of total α-SMA$^+$ area using whole PDAC tissue sections ($n = 43$) from an independent patient cohort.

PDAC and analyze impacts on the tumor microenvironment. Crossing mice with a Cre-inducible diphtheria toxin receptor allele (*Rosa26*$^{LSL\text{-}Hbegf/+}$, iDTR hereafter; ref. 47) into our *Fabp4-Cre;Rosa26*^{mTmG} model together with diphtheria toxin (DT) treatment would lead to ablation of PSC-derived CAFs. However, there were two obvious limitations of this model to overcome. First, as *Fabp4-Cre* mice feature high Cre activity in adipose tissue, this strategy would lead to systemic ablation of adipocytes, confounding the interpretation of results. Second, during characterization of our model, we noted a small population of CD45$^+$GFP$^+$ cells (about 2% of total intratumoral leukocytes; Supplementary Fig. S3A), which would also be targeted for ablation with this strategy. Notably, we did not observe CD45$^+$GFP$^+$ cells in normal pancreas of *Fabp4-Cre;Rosa26*^{mTmG} mice, suggesting that this Fabp4-expressing leukocyte population gets recruited into the tissue during tumor progression. To address these limitations and enable specific targeting of PSC-derived CAFs, we adapted published methods for retrograde ductal injection of viral particles directly into the pancreas (48, 49). This viral transduction approach achieves spatial control, limiting Fabp4-Cre to the pancreas and negating effects on adipose tissue, the hematopoietic system, and other potential cell or tissue types with Fabp4-driven Cre activity; this also enables somatic introduction of Fabp4-Cre in the adult mouse. To achieve this, we identified a minimal Fabp4 promoter and enhancer element that is highly active in primary PSCs but small enough to fit upstream of Cre within an adeno-associated virus (AAV) vector (see Methods). During pilot experiments, we found KP1 to be an optimal serotype to transduce PSCs *in vivo*, such that ductal injection of AAVKP1-Fabp4-Cre resulted in PSC labeling to a similar extent to that seen in mice harboring a *Fabp4-Cre* allele (Fig. 4A).

We next moved to tumor modeling, for which we subjected *Rosa26*$^{mTmG/iDTR}$ mice to a single surgery, including ductal injection of AAVKP1-Fabp4-Cre and orthotopic injection of KPC PDAC cells (Fig. 4B). Established tumors in this model harbored the expected frequencies of GFP$^+$ CAFs and lacked CD45$^+$GFP$^+$ cells (Supplementary Fig. S3B). We suspect that the GFP$^+$ cells lacking PDPN expression are quiescent or not fully activated PSCs, as these cells acquire PDPN expression upon activation to a CAF phenotype. To assess the functions of PSC-derived CAFs directly, as opposed to secondary impacts on other cells in the tumor microenvironment, we established tumors in our *Rosa26*$^{mTmG/iDTR}$ hosts transduced with AAVKP1-Fabp4-Cre and enrolled animals when tumors reached 5 to 6 mm in diameter by high-resolution ultrasound to treatment with vehicle or DT for 5 days to acutely ablate PSC-derived CAFs and harvested tumor tissue for analysis. This duration of PSC ablation did not visibly disrupt histology of normal pancreas or PDAC (Supplementary Fig. S3C). Consistent with selective targeting of a numerically minor CAF population, the DT-treated tumors retained high levels of CAFs, including those expressing α-SMA (Fig. 4C). Based on our transcriptional profiling, we analyzed ECM components enriched in PSC-derived CAFs and found TNC (Fig. 4D; Supplementary Fig. S3D) significantly reduced upon PSC-derived CAF ablation. Total collagen abundance remained unchanged (Supplementary Fig. S3E), together suggesting that PSC-derived CAFs regulate specific components of the ECM. Consistent with a broader role in ECM regulation and mechanosignaling, phospho-myosin light chain 2 (p-MLC2) was markedly reduced upon ablation of PSC-derived CAFs, consistent with cells being under decreased tension (Fig. 4E). Further analysis of these tumor tissues by second harmonic generation (SHG) revealed that fibrillar collagen abundance was modestly reduced upon PSC-derived CAF ablation, but this was not statistically significant (Fig. 4F and G). To assess tumor stiffness directly, we measured Young's modulus in control and PSC-depleted PDAC by atomic force microscopy. Tumors were significantly softer upon ablation of the numerically minor PSC-derived CAF population [Fig. 4H and I; Young's modulus for control = 1.02 ± 0.02 kPa, PSC-depleted = 0.74 ± 0.04 kPa; normal murine pancreas ≈0.50 kPa (50)]. As tumor stiffness and tumor-promoting mechanosignaling have been shown to be facilitated in part by focal adhesion kinase (FAK) signaling in PDAC (18, 51), we analyzed levels of phospho-FAK (Y397) and found that these signaling events were markedly reduced upon PSC-derived CAF ablation (Fig. 4J). We also assessed proliferation, apoptosis, and abundance of immune populations linked to CAF function, including CD8$^+$ T cells and myeloid cells after acute PSC-derived CAF ablation. We did not observe significant differences in proliferation or apoptosis in the epithelial or CAF compartment, nor did we find differences in CD8$^+$ T-cell frequencies, whereas CD68$^+$ myeloid cell abundance was significantly albeit modestly reduced with PSC-derived CAF ablation (Supplementary Fig. S3F–S3I). However, we do not exclude a functional relationship between PSC-derived CAFs and these features of the tumor microenvironment over

Figure 4. Targeted ablation reveals unique roles for PSC-derived CAFs in regulation of the ECM and mechanosignaling. **A,** IHC staining and quantification of GFP$^+$ cells in normal pancreas tissue from *Fabp4-Cre;Rosa26*^{mTmG} mice and from *Rosa26*$^{mTmG/iDTR}$ mice 7 days after intraductal injection with AAVKP1-Fabp4-Cre ($n = 5$). Data are presented as mean ± SEM. Scale bar, 50 μm. **B,** Schematic of tumor modeling using intraductal injection of AAVKP1-Fabp4-Cre and orthotopic transplantation of KPC PDAC cells into *Rosa26*$^{mTmG/iDTR}$ hosts. **C,** IHC staining for GFP, PDPN, and α-SMA of KPC FC1199 PDAC in *Rosa26*$^{mTmG/iDTR}$ hosts with intraductal injection of AAVKP1-Fabp4-Cre, enrolled when tumors reached 5 to 6 mm in diameter and treated with PBS or DT for 5 days ($n = 4$). Scale bar, 20 μm. **D,** IHC staining for TNC of KPC FC1199 PDAC in AAVKP1-Fabp4-Cre–injected *Rosa26*$^{mTmG/iDTR}$ hosts, enrolled at 5 to 6 mm in tumor diameter and treated with PBS or DT for 5 days ($n = 3$). Scale bar, 50 μm. Data are presented as mean ± SEM. **E,** IHC staining for p-MLC2 of PDAC samples as described in **D**. Scale bar, 50 μm. Data are presented as mean ± SEM. Quantification (**F**) and images (**G**) of fibrillar collagen content analyzed by second harmonic generation with normalized intensity as a quantification of concentration in control and PSC-depleted PDAC ($n = 3$ per group). Scale bar, 42.5 μm. **H,** Force maps generated by atomic force microscopy (AFM) on KPC FC1199 PDAC in AAVKP1-Fabp4-Cre–injected *Rosa26*$^{mTmG/iDTR}$ hosts ($n = 3$ per treatment group, control: 1,063 data points, depleted: 717 data points), excised after 5 days of treatment with PBS or DT. **I,** Quantification of Young's modulus per AFM measurements on control and PSC-depleted PDAC as described in **F**. The dashed line on the graph to the right denotes the approximate stiffness of normal murine pancreas tissue. **J,** IHC staining for p-FAK (Y397) of control and PSC-depleted PDAC harvested after 5 days of depletion ($n = 3$). Scale bar, 50 μm. Data are presented as mean ± SEM. **K,** Kaplan–Meier plot depicting overall survival of patients with PDAC with high versus low expression of a PSC-derived CAF ECM gene signature comprising 99 genes (see Methods), plotting the upper versus lower quartile ($n = 73$ per arm). *, $P < 0.05$; ****, $P < 0.0001$ by unpaired *t* test; ns, not significant.

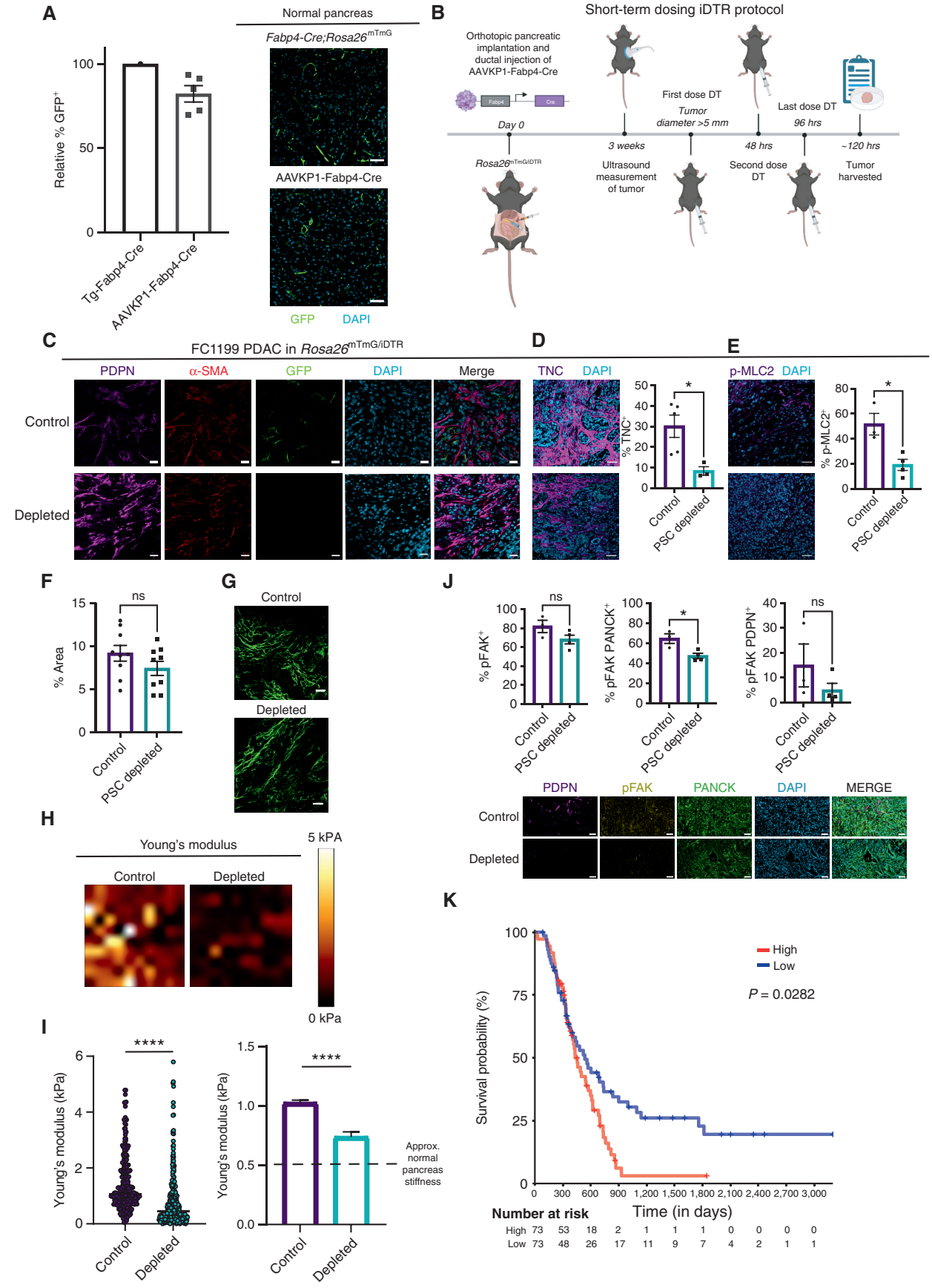
A
Normal pancreas
Fabp4-Cre;Rosa26mTmG
AAVKP1-Fabp4-Cre
Relative % GFP+
Tg-Fabp4-Cre
AAVKP1-Fabp4-Cre
GFP DAPI
B
Short-term dosing iDTR protocol
Orthotopic pancreatic implantation and ductal injection of AAVKP1-Fabp4-Cre
Day 0
Rosa26mTmG/iDTR
3 weeks
Ultrasound measurement of tumor
First dose DT
Tumor diameter >5 mm
48 hrs
Second dose DT
Last dose DT
96 hrs
~120 hrs
Tumor harvested
C
FC1199 PDAC in Rosa26mTmG/iDTR
PDPN α-SMA GFP DAPI Merge
Control
Depleted
D
TNC DAPI
% TNC+
Control
PSC depleted
E
p-MLC2 DAPI
% p-MLC2+
F
% Area
ns
G
Control
Depleted
H
Young's modulus
5 kPa
0 kPa
I
Young's modulus (kPa)
****
Approx. normal pancreas stiffness
J
% pFAK+
% pFAK PANCK+
% pFAK PDPN+
PDPN pFAK PANCK DAPI MERGE
K
Survival probability (%)
High
Low
P = 0.0282
Number at risk
Time (in days)
High 73 53 18 2 1 1 1 0 0 0 0
Low 73 48 26 17 11 9 7 4 2 1 1

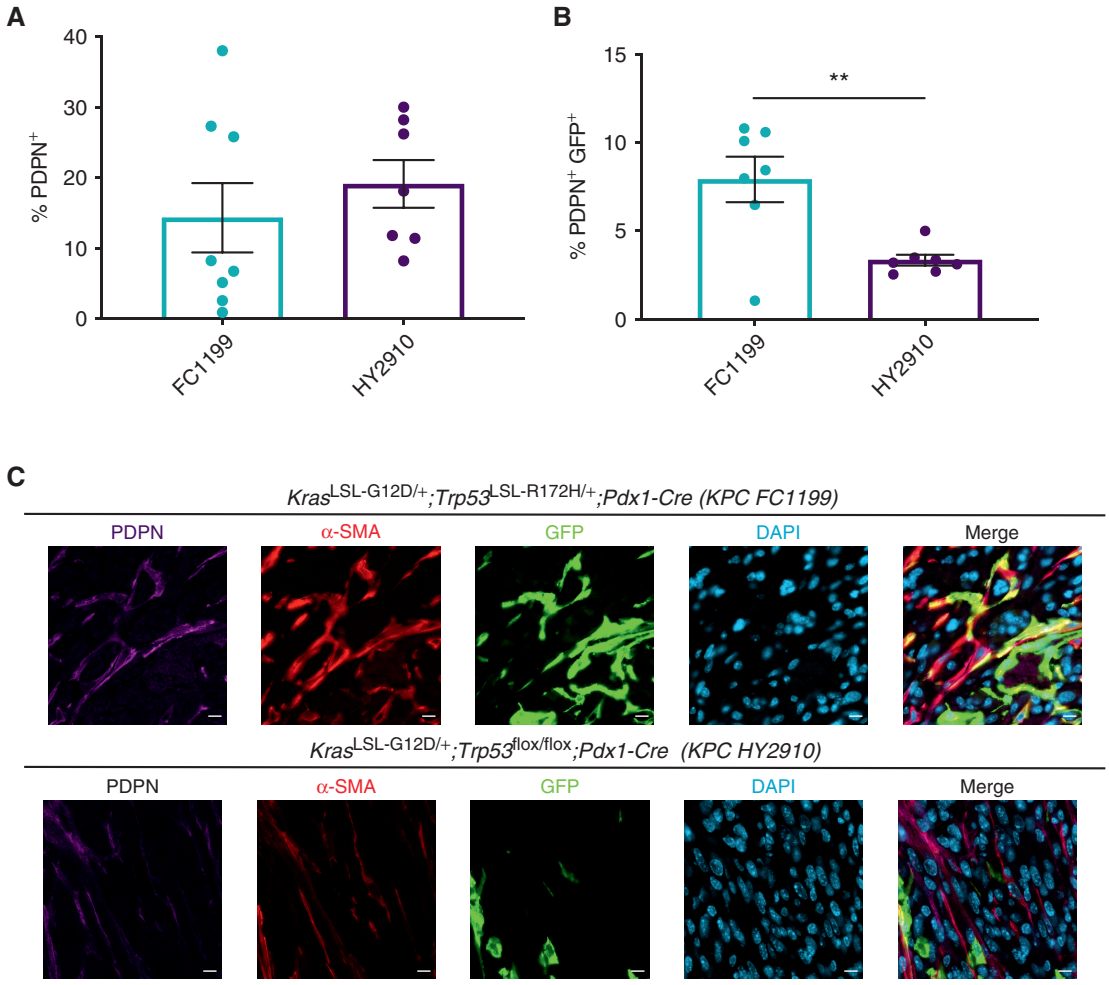

Figure 5. Tumor genotype with respect to p53 status influences stromal evolutionary routes. **A,** Flow cytometry analysis of PDPN+ cells in size-matched KPC FC1199 (p53 R172H, $n = 8$) and HY2910 (p53-null, $n = 7$) PDAC in *Fabp4-Cre;Rosa26*^{mTmG} hosts. Data are presented as mean ± SEM. **B,** Flow cytometry analysis of PDPN, GFP, and tdTomato in the tumors described in **A** to quantify the percentage of CAFs derived from PSCs. Data are presented as mean ± SEM. **C,** IHC staining for GFP and PDPN on KPC FC1199 and HY2910 PDAC in *Fabp4-Cre;Rosa26*^{mTmG} hosts ($n = 3$). Scale bar, 10 μm. (*continued on following page*)

time. These results suggest that PSC-derived CAFs drive the establishment of a tumor-promoting desmoplastic milieu. We therefore developed an ECM signature specific to or enriched among PSC-derived CAFs per our RNA-seq datasets and tested its prognostic value. Although collagen and bulk tumor stromal density are associated with a better prognosis in PDAC (25, 27), this PSC-associated ECM signature was associated with a worse prognosis among patients with PDAC (Fig. 4K; Supplementary Table S2). These results suggest that PSCs give rise to CAFs, which regulate specific features of the stromal microenvironment associated with PDAC aggressiveness.

Relationship between Tumor Genotype and Stromal Evolutionary Routes with Respect to CAF Origins

Our results in patients with PDAC suggested heterogeneity in PSC-derived CAF frequencies and led us to question whether tumor genotype regulates stromal evolution from distinct cells of origin. In support of this notion, we observed significantly elevated *Hspg2* (perlecan) expression in PSC-derived CAFs compared with CAFs of other origins, raising the possibility that previously reported distinctions between CAFs associated with p53-mutant versus p53-null PDAC (46) reflect differential recruitment of PSCs into the CAF pool. To begin to test a relationship between cancer cell–intrinsic p53 status and stromal evolution, we compared two PDAC models from the same genetic background (C57BL/6J) and the same driver mutation in KRAS (G12D), but one featuring p53 R172H and the other featuring p53 loss. We harvested size-matched tumors from these models in *Fabp4-Cre;Rosa26*^{mTmG} hosts and found that total PDPN+ CAF frequencies were not different (Fig. 5A), but that PSCs made a significantly lower contribution to the CAF population in the context of p53-null PDAC (Fig. 5B and C). To assess a causal role for p53 status in the regulation of stromal evolution, we generated isogenic models by using Cas9 and two different single-guide RNAs targeting *Trp53* to knock out p53 in a p53-mutant

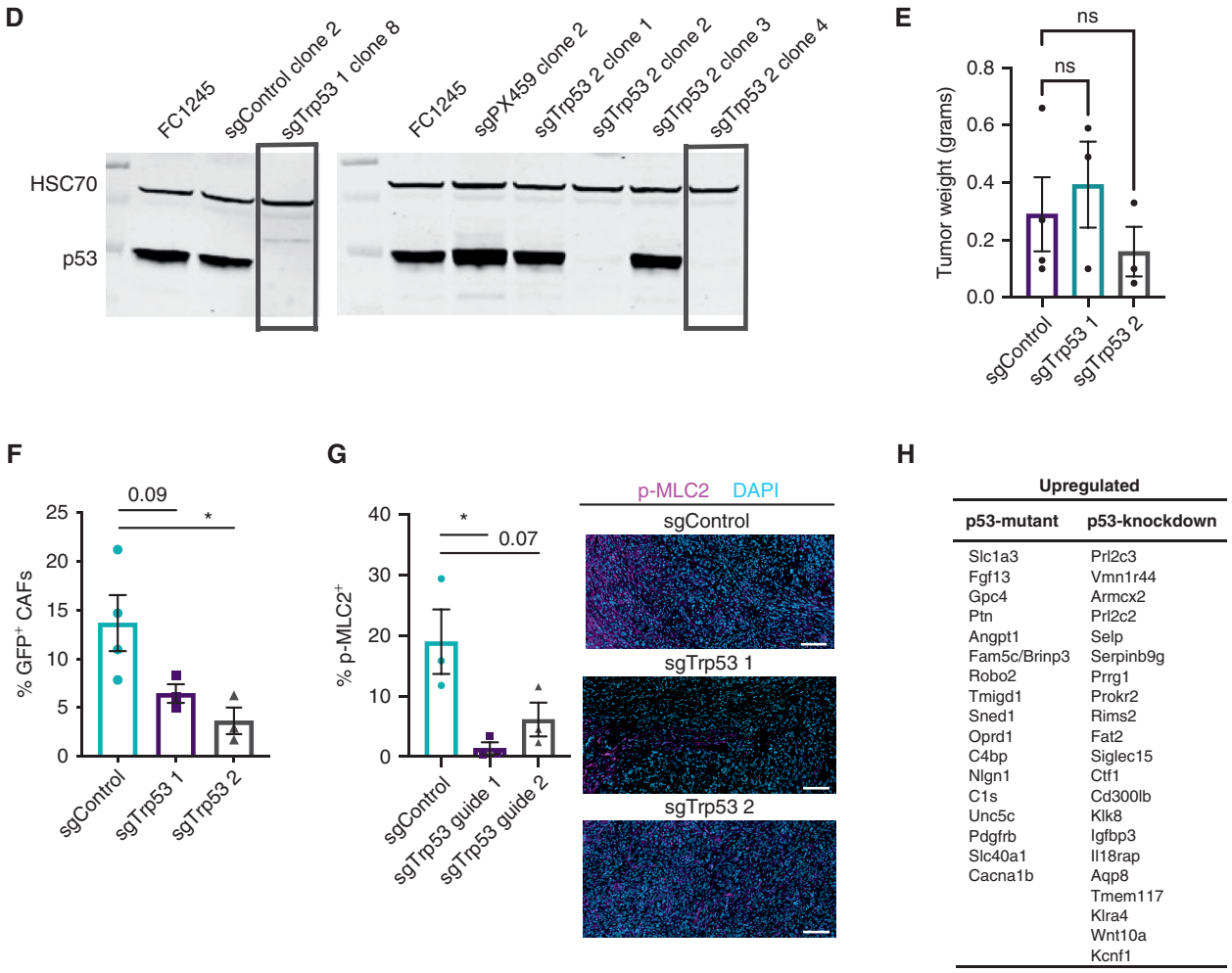

Upregulated

p53-mutant	p53-knockdown
Slc1a3	Prl2c3
Fgf13	Vmn1r44
Gpc4	Armcx2
Ptn	Prl2c2
Angpt1	Selp
Fam5c/Brinp3	Serpinb9g
Robo2	Prrg1
Tmigd1	Prokr2
Sned1	Rims2
Oprd1	Fat2
C4bp	Siglec15
Nlgn1	Ctf1
C1s	Cd300lb
Unc5c	Klk8
Pdgfrb	Igfbp3
Slc40a1	Il18rap
Cacna1b	Aqp8
	Tmem117
	Klra4
	Wnt10a
	Kcnf1

Figure 5. ***(Continued)*** **D,** Western blots for p53 and HSC70 (loading control) using whole-cell lysates from parental KPC FC1245 (p53 R172H) cells or derivative lines transfected with control plasmid or one of two sgTrp53 sequences. Boxes indicate clones selected for experimentation. **E,** Tumor weights at experimental endpoint from control and sgTrp53 PDAC in *Fabp4-Cre;Rosa26*^{mTmG} hosts. **F,** Flow cytometry analysis of PDPN, GFP, and tdTomato in size-matched control ($n = 4$) and sgTrp53 ($n = 3$ per line) PDAC in *Fabp4-Cre;Rosa26*^{mTmG} hosts. Data are presented as mean ± SEM. **G,** IHC staining for p-MLC2 in size-matched control and sgTrp53 PDAC in *Fabp4-Cre;Rosa26*^{mTmG} hosts ($n = 3$). Scale bar, 100 μm. **H,** List of candidate secreted factors differentially expressed in p53-mutant versus p53-null PDAC cells. *, $P < 0.05$; **, $P < 0.01$ by one-way ANOVA; ns, not significant.

(R172H) parental line (Fig. 5D). We then transplanted these lines in pancreata of *Fabp4-Cre;Rosa26*^{mTmG} mice, harvested size-matched tumors (Fig. 5E), and analyzed CAF lineages by flow cytometry. We found that loss of p53 led to a reduction of PSC-derived CAF frequencies out of total PDPN$^+$ CAFs (Fig. 5F), although we note that, for one of the p53-null lines, this trend did not reach statistical significance. Furthermore, although p53-null tumors harbored a substantial CAF population as expected, p-MLC2 abundance was significantly reduced compared with p53-mutant tumors (Fig. 5G), consistent with a previous study (46) and with reduced PSC-derived CAF frequencies. To identify candidate p53-regulated factors that promote or suppress PSC activation, we probed RNA-seq data from a recent study comparing KPC PDAC cells in which p53 was knocked down with short hairpin RNA to parental p53-mutant controls (52). Of the top 40 up- or downregulated genes in p53-knockdown cells, we identified 17 genes upregulated in p53-mutant controls and 21 genes upregulated in p53-knockdown cells that encode secreted factors (soluble or membrane associated) that may participate in paracrine interactions with the stroma (Fig. 5H). These results suggest that cancer cell–derived factors stimulate stromal evolution and that PDAC of distinct genotypes may be differentially responsive to stroma-targeted therapies independent of stromal density as a consequence of distinct mesenchymal cells of origin.

DISCUSSION

The discovery of stellate cells in the pancreas in 1998 provided a crucial basis for our understanding of the cellular source(s) of pancreatic fibrosis (42). As HSCs serve as the dominant cellular source of fibrosis in the context of liver injury (35) and PSCs were shown to have similar fibrogenic

potential to their counterparts in the liver (32), it was reasonable to speculate that PSCs are the cellular source of pancreatic fibrosis and of the extensive desmoplastic reaction in PDAC (31). Indeed, activation of PSCs in culture leads to induction of a transcriptional program consistent with CAF features (39), and more recently, PSCs were shown to give rise to the previously defined iCAF and myCAF subtypes in culture upon exposure to defined soluble cues and growth substrates (38). In light of the plasticity of this cell type and the cells' presumed role as dominant contributors to the PDAC stroma, we expected that our genetic means to track and ablate PSCs and derivative CAFs would target most or all CAFs in the PDAC microenvironment. We were surprised to find that PSCs give rise to only a small minority of CAFs in PDAC, with frequency dependent in part on tumor genotype. As we come to further understand the functions of this CAF population, we will further analyze clinical cohorts, leveraging heterogeneity in PSC-derived CAF frequency among patient samples to investigate potential stratification strategies or tailored therapies informed by CAF cell of origin. Although we acknowledge a lack of mechanistic data in our study, the central observation is of importance to our understanding of pancreatic cancer stromal evolution and may serve as the basis for upcoming mechanistic studies aimed to identify specific tumor-promoting functions of this defined CAF population.

As PSC-derived CAFs have a transcriptional profile distinct from CAFs of other origins, our results in the context of the recent literature suggest that CAF transcriptional heterogeneity results from (at least) two sources: signaling gradients differentially regulating common cells of origin and mesenchymal lineage heterogeneity. The results of our PSC-derived CAF ablation experiments suggest that functional heterogeneity underlies transcriptional heterogeneity. Although transcriptional and phenotypic plasticity among CAFs likely poses some limitations to the feasibility of targeting specific subsets therapeutically, our model enabling targeted ablation of a defined CAF subset raises the possibility that CAF subsets have sufficient functional distinctions that targeting these subsets in preclinical models, to understand their role in PDAC biology, and differentially targeting them therapeutically may indeed be possible. This notion is supported by a recent study revealing that myCAFs are differentially dependent on the Hedgehog pathway (20) such that Hedgehog inhibition markedly skewed the PDAC CAF population to reduce myCAFs and increase iCAFs. Additional impacts on tumor-infiltrating T cells suggest potential immune-suppressive functions of iCAFs. Thus, as the unique functions of these distinct CAF subsets further come to light, targeting specific CAFs may emerge as viable combination therapeutic strategies. It will be important to extend the functional analyses performed here to additional CAF populations, pending development of relevant models, to better understand their distinct roles in the tumor microenvironment and inform us about potential targets for therapeutic intervention.

The high α-SMA expression and ECM production characteristic of PSC-derived CAFs suggest that they fall within the previously described myCAF (11, 28) or TGFβ CAF (12) population. However, as total collagen abundance remains unchanged and α-SMA$^+$ CAFs remain highly abundant upon PSC-derived CAF ablation, this numerically minor population seems to be but a subset of the broader myCAF pool. CAFs in several tumor types fall into functionally distinct FAP^{HI} and α-SMA^{HI} subtypes: FAP^{HI} CAFs predominantly synthesize and remodel ECM, whereas α-SMA^{HI} CAFs mediate contraction (53). This heterogeneity is governed by substratum and ECM composition, which are in turn regulated by CAF phenotypes. Our results suggest that PSCs give rise to CAFs in both of these functional categories, and single-cell sequencing approaches will be helpful in assessing the relative contribution to each category. As PSC-derived CAFs regulate specific ECM components and biophysical properties implicated in tumor aggressiveness and metastatic progression (18, 46), we speculate that PSCs give rise to a tumor-promoting myCAF subset, to be investigated in depth in subsequent studies. However, in light of the apparent dependency of myCAFs on Hedgehog signaling and the detrimental effects of long-term genetic or pharmacologic SHH inhibition (23, 24), it seems likely that another subset of myCAFs is tumor suppressive and promotes a more differentiated and less aggressive PDAC phenotype. The tumor-suppressive potential of other myCAF constituents is consistent with prior studies providing correlative evidence for heightened immune suppression upon reduction in overall myCAF frequency in the PDAC microenvironment (13, 20). These tumor-suppressive CAF populations and their homeostatic or beneficial functions will be important to identify, as maintaining these functions should be a goal of future stroma-targeted therapies.

As our data define PSCs as numerically minor contributors to the CAF population, an important question to address is the cellular origin of most PDAC CAFs. Analysis of single-cell RNA-seq data from murine PDAC together with publicly available transcriptional profiles suggests that the previously described apCAFs in fact derive from mesothelial cells (12). As for the remaining CAFs, including iCAFs and the non–PSC-derived myCAFs, the origins remain unclear but may come from pancreas-resident fibroblast populations or potentially from the bone marrow. Whereas bone marrow–derived mesenchymal stromal cells are important contributors to the CAF population in other cancer types, including breast cancer (54), the contribution of bone marrow progenitors to PDAC CAFs remains to be determined. Importantly, a recent study employed lineage tracing and identified two distinct fibroblast populations in normal pancreas tissue, one marked by the Hedgehog-responsive transcription factor Gli1 and the other by the tissue-restricted mesenchymal transcription factor Hoxb6 (55). These factors label distinct fibroblast populations in the pancreas, which are similar in frequency, but in the early stages of pancreatic carcinogenesis, the Gli1$^+$ fibroblast population expands considerably, whereas the Hoxb6$^+$ population does not, such that the pancreas-resident Gli1$^+$ fibroblasts are major contributors to the stroma associated with precursor lesions. Although our study is limited to transplantable PDAC models, analysis of stromal evolution in autochthonous models will be important to identify alterations in stromal composition throughout stepwise tumorigenesis. Future studies to define the mechanisms

shaping PDAC CAF heterogeneity and the unique functions of distinct CAF subsets will improve our understanding of how the tumor microenvironment affects PDAC progression and perhaps point to important stromal targets for therapeutic intervention.

METHODS

Animals

All experiments performed in mice were reviewed and overseen by the Institutional Animal Care and Use Committee at Oregon Health & Science University (OHSU) in accordance with NIH guidelines for the humane treatment of animals. *Fabp4-Cre* (005069) and *Rosa-26*^{mTmG} (007676) mice from The Jackson Laboratory were used for PSC analyses and orthotopic transplantation experiments at 8 to 12 weeks of age, including male and female mice. *Rosa26*^{mTmG} and iDTR (007900) mice from The Jackson Laboratory were used for retrograde ductal injection and orthotopic transplantation for PSC ablation experiments at 8 to 12 weeks of age, including male and female mice.

Human Tissue Samples

Human patient PDAC tissue samples donated to the Oregon Pancreas Tissue Registry program with informed written patient consent [Institutional Review Board (IRB) approved, IRB00003609], in accordance with full ethical approval by the OHSU IRB, were provided by the OHSU Brenden-Colson Center for Pancreatic Care and the Knight BioLibrary upon pathology review by Dr. Rosemary Makar and secondary review by Dr. Christopher Corless.

The PDAC tumor microarray was described previously (56). Human PDAC specimens were obtained from patients who underwent surgical resection of primary PDAC, under IRB-approved protocol IRB11–000512. This study was conducted under strict compliance with institutional ethical regulations. The study had minimal risk per the IRB protocol, and thus informed consent was not necessary.

PSC Isolation and Analysis

PSCs were isolated from healthy pancreas tissue from 8-week-old *Fabp4-Cre;Rosa26*^{mTmG} mice as previously described (39). Upon retrieval from the density gradient interface, PSCs were plated on glass coverslips in DMEM containing 10% FBS. On day 2 of culture, cells were fixed in 4% paraformaldehyde for 15 minutes at room temperature, washed three times with PBS, and permeabilized with 0.1% Triton X-100 for 10 minutes at room temperature. Following permeabilization, coverslips were blocked for 1 hour at room temperature in blocking solution (8% BSA), and then transferred to a carrier solution (1% BSA) containing diluted antibodies against desmin and GFP (desmin: Cell Signaling Technology, D93F5; GFP: Cell Signaling Technology, 4B10). Coverslips were incubated with the primary antibody solution for 3 hours at room temperature and then washed five times for 5 minutes each in PBS. Secondary Alexa Fluor–conjugated secondary antibodies were diluted in the same carrier solution (1:400) and added to the coverslips for 1 hour at room temperature. Coverslips were then washed five times for 5 minutes each in PBS and mounted with VECTASHIELD (Vector Labs) mounting medium containing DAPI. Cells were imaged using the LSM 880 confocal microscope (Carl Zeiss) described above, and costained cells out of total desmin-positive cells were scored manually.

Cell Culture

FC1199 and FC1245 (provided by Dr. David Tuveson), 4662 (provided by Dr. Robert Vonderheide), and HY2910 (provided by Dr. Haoqiang Ying) PDAC cell lines were derived from primary murine PDAC. Cell lines were routinely passaged in DMEM (Thermo Fisher Scientific) containing 10% FBS (HyClone) for no more than 25 to 30 passages. Primary PSCs were also cultured in DMEM containing 10% FBS after isolation from mouse pancreas and until fixation and analysis. Cell lines were routinely tested for *Mycoplasma* at least monthly (MycoAlert Detection Kit, Lonza). Cell line authentication was not performed.

IHC

For mouse tissue harvest, mice were anesthetized and euthanized according to institutional guidelines. Pancreas tissue or tumors were excised carefully and fixed overnight in 10% neutral buffered formalin or embedded in optimal cutting temperature (OCT) compound and frozen at –80°C. Fixed tissues were paraffin embedded, sectioned, deparaffinized, and rehydrated through an ethanol series and ultimately in PBS. Following antigen retrieval, tissue samples were blocked for 2 hours at room temperature in blocking solution (8% BSA) and transferred to a carrier solution (1% BSA) containing diluted antibodies. Sections were incubated overnight at room temperature and then washed five times for 5 minutes each in PBS. Secondary Alexa Fluor–conjugated antibodies diluted in the same carrier solution (1:200) were added to the sections for 2 hours at room temperature. Sections were then washed five times for 5 minutes each in PBS, autofluorescence quenched with the TrueVIEW reagent (Vector Laboratories), stained with DAPI, and mounted with VectaShield mounting medium. Fresh-frozen tissues were sectioned, fixed, and used to stain for CD45 in FC1199 tumors and for NG2 in normal pancreas tissue, then counterstained with DAPI-containing VECTASHIELD mounting medium for fluorescence microscopy. Antibodies used for IHC were as follows: CD31 (Abcam, ab28364), GFP [Cell Signaling Technology, 4B10 (mouse) or D5.1 (rabbit)], CD45 (Abcam, ab25386), NG2 (EMD Millipore, AB5320), α-SMA (Thermo Fisher Scientific, MA511547), PDPN (Thermo Fisher Scientific, 14–5381–81), TIE1 (Abcam, ab111547, mouse tissues; Supplementary Fig. S2B), TIE1 (Biorbyt, orb11476, mouse tissues; Supplementary Fig. S2C), TIE1 (Thermo Fisher Scientific, PA527903, human tissues), TNC (Abcam, ab108930), p-MLC2 (Cell Signaling Technology, 3674), pFAK (Thermo Fisher Scientific, 700255), Ki-67 (Cell Signaling Technology, 12202), CC3 (Cell Signaling Technology, 9664), CD8 (Abcam, ab203035), and CD68 (Abcam, ab125047). Stained tissues were imaged using a laser-scanning confocal inverted microscope (LSM 880, Carl Zeiss), and a 40×/1.1 NA water objective or 63×/1.4 NA oil objective was used to image the samples. Slides were scanned using a Zeiss Axio Scan.Z1 and quantified using QuPath or Aperio software.

For quantification of TIE1/α-SMA colocalization on human PDAC sections, images were acquired on an AxioScan.Z1 using a 10×/0.45 NA plan-apochromat lens. Fluorochromes were excited with a Colibri 7 light source (Carl Zeiss), and excitation and emission light was passed through the following Zeiss filter sets for the appropriate channel: DAPI, 96 HE; Alexa Fluor 488, 38 HE; and Alexa Fluor 594, 71 HcRed. Images were analyzed for colocalization in ZEN v2.3 (Carl Zeiss). Thresholds for the AF594 and AF488 channels were set by eye for each slide (three slides total) for the tissue microarray analysis. Within each slide, the same thresholds were used across all tissues. Dynamic range was set to a 14-bit image (16,384 maximum intensity).

FACS and Flow Cytometry

For flow cytometry analysis of normal pancreas tissue, pancreata were harvested, briefly minced with scissors, and digested with 0.02% Pronase (Sigma-Aldrich), 0.05% Collagenase P (Sigma-Aldrich), and 0.1% DNase I (Sigma-Aldrich) in Gey's balanced salt solution (GBSS; Sigma-Aldrich) at 37°C for 20 minutes. After dissociation, tissue was triturated until large pieces were no longer visible, and the resulting cell suspension was filtered through a 100-μm nylon mesh. Cells were then washed with GBSS, pelleted, subject to red blood cell lysis

in ACK lysis buffer (Thermo Fisher Scientific) for 3 minutes at room temperature, washed in FACS buffer (PBS containing 2% FBS), pelleted, and resuspended in FACS buffer for flow cytometry to analyze vitamin A positivity based on autofluorescence using the 405-nm laser on a BD LSRFortessa flow cytometer. To analyze endothelial cells, following red blood cell lysis, cells were incubated with CD16/CD32 antibody (BD Biosciences, 553141) to block Fc receptors for 2 minutes at room temperature and then stained with a PerCP/Cy5.5-conjugated CD31 antibody (BioLegend, 102522) for 30 minutes on ice. Stained cells were washed with cold FACS buffer, pelleted, and resuspended in cold FACS buffer for flow cytometry analysis.

For analytic flow cytometry or FACS on PDAC tissues, tumors were harvested, minced with scissors, and dissociated in DMEM containing 1 mg/mL Collagenase IV (Thermo Fisher Scientific), 0.1% Soybean Trypsin Inhibitor (Thermo Fisher Scientific), 50 U/mL DNase I (Sigma-Aldrich), and 0.125 mg/mL Dispase II (Thermo Fisher Scientific) at 37°C for 1 hour. Digested tissues were pelleted, resuspended in 0.25% trypsin in DMEM, and incubated at 37°C for 10 minutes and then washed with cold DMEM containing 10% FBS and pelleted. Resuspended cells were filtered through a 100-μm cell strainer, pelleted, washed with DMEM + 10% FBS, and pelleted again. Cells were resuspended in ACK lysis buffer as described above, washed with FACS buffer, pelleted, and resuspended in FACS buffer. Fc block was performed as described above, and then cells were stained with antibodies for 30 minutes on ice: biotinylated anti-PDPN (BioLegend, 127404), biotinylated anti-PDGFRα (anti-CD140a; BioLegend, 135910), PerCP/Cy5.5-conjugated anti-CD31 (BioLegend, 102522), and/or PE/Cy7-conjugated anti-CD45 (BioLegend, 103113). Cells were then washed with FACS buffer and pelleted. Biotinylated antibodies were incubated with APC Streptavidin (BD 554067) for 30 minutes on ice, washed with FACS buffer, pelleted, and resuspended in FACS buffer. After staining for the purpose of CAF sorting and subsequent RNA-seq, RNase inhibitor (New England Biolabs, M0314, 1:40) was added to the cell suspension and CAFs were sorted into TRIzol LS (Thermo Fisher Scientific). Flow cytometry analysis was performed on a BD LSRFortessa, while CAF sorting was performed on a BD FACSAria Fusion. Flow cytometry data were analyzed with FlowJo software. GFP^+ or $tdTomato^+$ CAF frequencies were calculated out of the total GFP^+ plus $tdTomato^+$ population, excluding any cells lacking either lineage label that represents tumor cells.

Orthotopic PDAC Experiments

Male and female mice at 8 to 12 weeks of age were used as hosts for PDAC orthotopic transplantation, using genotypes described in the Results section and figure legends. Mice were anesthetized with ketamine and xylazine, and pancreata were injected with 5×10^3 FC1199 or FC1245 cells (provided by Dr. David Tuveson), 1×10^5 4662 cells (provided by Dr. Robert Vonderheide), or 1×10^4 HY2910 cells (provided by Dr. Haoqiang Ying), all derived from primary PDAC in *Kras*$^{LSL\text{-}G12D/+}$;*Trp53*$^{LSL\text{-}R172H/+}$;*Pdx1-Cre* mice (FC1199, FC1245, 4662) or *Kras*$^{LSL\text{-}G12D/+}$;*Trp53*$^{flox/flox}$;*Pdx1-Cre* mice (HY2910) of a C57BL/6J genetic background. Orthotopic transplantation was performed as previously described (57). For PSC-derived CAF ablation experiments, pancreata were imaged beginning 14 days after transplantation by high-resolution ultrasound using the Vevo 770 imaging system; mice were enrolled in the study when tumors reached 5 to 6 mm in diameter. Enrolled mice were treated with sterile PBS or 25 ng/g DT (List Biological Laboratories) by intraperitoneal injection every 2 days, and tumors were harvested on day 5 postenrollment for analysis.

Retrograde Ductal AAV Delivery

A promoter and enhancer element upstream of mouse *Fabp4* (Addgene, 8858) was cloned into pAAV-iCre-WPRE (Vector Biosystems) upstream of Cre. KP1-serotyped AAV-Fabp4-Cre was generated and titered by the OHSU Molecular Virology Core. AAVKP1-Fabp4-Cre viral stock was diluted to 1×10^{10} viral genomes/mL in 10 μg/mL DEAE-Dextran (Sigma-Aldrich) in PBS, incubated for 30 minutes at room temperature, and then placed on ice. Retrograde ductal injections were performed as previously described (48). Mice were anesthetized with ketamine and xylazine until nonresponsive to toe pinch. Feet were taped down with surgical tape on a sterile mat. Entire abdomen was shaved and the shaved area cleaned with 70% ethanol and betadine. A midline incision was made about 1 inch long, and incision edges were secured with hemostatic forceps. Nonweave sterile gauze was moistened with sterile PBS. Intestines were gently extracted using circle forceps and gently laid onto damp gauze. Intestines were slowly extracted until duct was visible. Exposed intestines were covered with damp gauze to keep moist, and sterile PBS was continually added throughout the procedure as necessary to keep gauze and tissue from drying out.

One microvascular clip was placed on the cystic duct near the gallbladder. The sphincter of Oddi was located; a 30-gauge insulin syringe was loaded with 100 μL viral solution (to inject 1×10^9 viral genomes per mouse) and the needle inserted through the sphincter of Oddi into the common bile duct up to its convergence with the cystic duct, about halfway to the clip. Viral solution was slowly injected over the course of 2 minutes. The needle was left in place for 30 seconds after completion of the injection, and then slowly and gently removed. The clip was then removed. Intestines were carefully returned to the abdomen, muscle layer was closed with Vicryl sutures, and skin was closed with sterile suture clips. When performed together with orthotopic transplantation of PDAC cells, cells were injected after removal of the syringe and clip.

Atomic Force Microscopy

Fresh tumor tissues were placed in the middle of a disposable cryomold and embedded in OCT compound. Tissues were sectioned with a cryostat at a thickness of 50 μm and adhered to positively charged microscope slides. Prior to measurements, samples were thawed at room temperature in DMEM/F-12 supplemented with 10% FBS and a protease inhibitor cocktail (Sigma-Aldrich, 11836170001). Atomic force microscopy measurements were performed with a NanoWizard 4 XP BioScience with HybridStage (Bruker) mounted on a Zeiss Axio Observer inverted optical microscope. Dulled triangular silicon nitride ScanAsyst-Fluid probes were used (κ = 0.7 N/m; Bruker) at a maximum applied force of 4 nN and approach speed of 5 μm/s. Each probe was calibrated with the thermal oscillation method prior to measurements on each tissue. Force curves were analyzed to obtain the Young's modulus using the JPK Data Processing Software package with the Hertz/Sneddon model assuming an incompressible tissue and a Poisson's ratio of 0.5 with tip parameters provided by the manufacturer's specifications. Three independent samples were imaged from each treatment group at three locations at varying tissue depths with a scan size of 100 μm^2, with force measurements spaced every 10 μm.

SHG Imaging and Analysis

Unfixed, hydrated control ($n = 3$) and PSC-depleted ($n = 3$) tumors embedded in OCT compound were sectioned at 15 μm thickness. The SHG images were acquired with a Zeiss LSM 780 multiphoton microscope mounted on a Zeiss Observer Z1 inverted microscope stand. Tissues were imaged with a Coherent Chameleon Vision II ultrafast pulsed infrared laser (680–1080 nm) tuned to 800 nm. A Zeiss 20× air objective (NA = 0.8) focused the beam onto the sample, and SHG imaging was detected from the back-scattered signal with a Gallium arsenide phosphide non-descanned detector. For image analysis, three representative fields of view were analyzed per sample. A minimal threshold in the SHG signal was set and maintained

across all images with ImageJ (NIH) and was used to obtain the percent area and normalized intensity.

Survival Analysis of a PSC ECM Gene Signature

The PSC-derived CAF ECM signature genes (Supplementary Table S2) were defined as the overlap of the genes annotated in the Reactome Extracellular Matrix Organization pathway and the upregulated genes in GFP$^+$ CAFs (FDR <0.01 and fold change >1.25) per our RNA-seq analysis. In the signature survival analysis, 297 samples were collected with survival time from the OHSU Brenden-Colson Center for Pancreatic Care Tempus dataset. The gene set variation analysis (GSVA) algorithm with the default settings, as implemented in the GSVA R package (version 1.34.0), was applied to calculate the gene signature score for each sample. Next, the samples were stratified into two groups based on the quantile values of the signature scores (upper quartile versus lower quartile). Survival curves of these two groups of patients were analyzed by Kaplan–Meier method with statistical significance calculated using the log-rank test. The Kaplan–Meier estimator and log-rank test were calculated in the survival R package (version 3.2–3).

Statistical Analysis

Statistical analyses were performed using GraphPad PRISM software (GraphPad Software). Student *t* test was used to compare two groups to each other. One-way ANOVA was performed when multiple conditions were compared for one variable. Tukey *post hoc* tests were used after ANOVA analyses to perform multiple group comparison. Analysis with a P value <0.05 was considered statistically significant.

Data Availability

All sequence data from this study have been deposited in the publicly available Gene Expression Omnibus under accession number GSE143805.

Authors' Disclosures

C.C. DuFort reports grants from the NIH/NCI during the conduct of the study. S.R. Hingorani reports grants from the NIH/NCI during the conduct of the study. M.H. Sherman reports personal fees from Autobahn Labs outside the submitted work. No disclosures were reported by the other authors.

Authors' Contributions

E.J. Helms: Conceptualization, resources, data curation, formal analysis, validation, investigation, visualization, methodology, writing–original draft, writing–review and editing. **M.W. Berry:** Resources, formal analysis, validation, investigation, writing–review and editing. **R.C. Chaw:** Data curation, formal analysis, visualization, writing–review and editing. **C.C. DuFort:** Data curation, formal analysis, investigation, writing–review and editing. **D. Sun:** Data curation, formal analysis, investigation, visualization, writing–review and editing. **M.K. Onate:** Resources, data curation, formal analysis, writing–review and editing. **C. Oon:** Resources, data curation, formal analysis, investigation, writing–review and editing. **S. Bhattacharyya:** Resources, data curation, formal analysis, validation, investigation, visualization, writing–review and editing. **H. Sanford-Crane:** Resources, formal analysis, investigation, writing–review and editing. **W. Horton:** Resources, data curation, formal analysis, investigation, visualization, writing–review and editing. **J.M. Finan:** Data curation, formal analysis, writing–review and editing. **A. Sattler:** Data curation, formal analysis, writing–review and editing. **R. Makar:** Formal analysis, investigation, writing–review and editing. **D.W. Dawson:** Resources, data curation, formal analysis, investigation, visualization, writing–review and editing. **Z. Xia:** Resources, data curation, formal analysis, supervision, investigation, visualization, writing–review and editing. **S.R. Hingorani:** Resources, data curation, formal analysis, supervision, investigation, visualization, writing–review and editing. **M.H. Sherman:** Conceptualization, resources, data curation, formal analysis, supervision, funding acquisition, validation, investigation, visualization, methodology, writing–original draft, writing–review and editing.

Acknowledgments

We thank all members of the Sherman lab, Jae Myoung Suh, and Sara Courtneidge for helpful conceptual input on this work and Markus Grompe, Hiroyuki Nakai, Shin-Heng Chiou, and Monte Winslow for guidance on the intraductal AAV delivery approach. This work was supported by the OHSU Molecular Virology Core, Knight BioLibrary (and particularly by operations supervisor Danielle Galipeau and by Christopher Corless in his capacity as chief medical officer of the Knight Diagnostic Laboratories), Flow Cytometry Shared Resource, Massively Parallel Sequencing Shared Resource, Advanced Light Microscopy Shared Resource, and Histopathology Shared Resource, with core facility support from the Knight Cancer Institute Cancer Center Support Grant P30 CA069533. Funding to support this study came from NIH grant T32 GM071338 (to E.J. Helms), NIH grants R01 CA161112 and U01 CA224193 (to S.R. Hingorani), and NIH grant R01 CA250917; DOD Peer Reviewed Cancer Research Program grant W81XWH-18–1-0437 (to M.H. Sherman); and a Pew-Stewart Scholar Award (to M.H. Sherman).

The publication costs of this article were defrayed in part by the payment of publication fees. Therefore, and solely to indicate this fact, this article is hereby marked "advertisement" in accordance with 18 USC section 1734.

Note

Supplementary data for this article are available at Cancer Discovery Online (http://cancerdiscovery.aacrjournals.org/).

Received May 8, 2021; revised August 12, 2021; accepted September 16, 2021; published first September 21, 2021.

REFERENCES

1. Biffi G, Tuveson DA. Diversity and biology of cancer-associated fibroblasts. Physiol Rev 2021;101:147–76.
2. Helms E, Onate MK, Sherman MH. Fibroblast heterogeneity in the pancreatic tumor microenvironment. Cancer Discov 2020;10:648–56.
3. Sahai E, Astsaturov I, Cukierman E, DeNardo DG, Egeblad M, Evans RM, et al. A framework for advancing our understanding of cancer-associated fibroblasts. Nat Rev Cancer 2020;20:174–86.
4. Maitra A, Hruban RH. Pancreatic cancer. Annu Rev Pathol 2008;3:157–88.
5. Sousa CM, Biancur DE, Wang X, Halbrook CJ, Sherman MH, Zhang L, et al. Pancreatic stellate cells support tumour metabolism through autophagic alanine secretion. Nature 2016;536:479–83.
6. Sherman MH, Yu RT, Tseng TW, Sousa CM, Liu S, Truitt ML, et al. Stromal cues regulate the pancreatic cancer epigenome and metabolome. Proc Natl Acad Sci U S A 2017;114:1129–34.
7. Zhu Z, Achreja A, Meurs N, Animasahun O, Owen S, Mittal A, et al. Tumour-reprogrammed stromal BCAT1 fuels branched-chain ketoacid dependency in stromal-rich PDAC tumours. Nat Metab 2020;2:775–92.
8. Zhao H, Yang L, Baddour J, Achreja A, Bernard V, Moss T, et al. Tumor microenvironment derived exosomes pleiotropically modulate cancer cell metabolism. Elife 2016;5:e10250.
9. Zhang Y, Recouvreux MV, Jung M, Galenkamp KMO, Li Y, Zagnitko O, et al. Macropinocytosis in cancer-associated fibroblasts is dependent

on CaMKK2/ARHGEF2 signaling and functions to support tumor and stromal cell fitness. Cancer Discov 2021;11:1808–25.
10. Francescone R, Barbosa Vendramini-Costa D, Franco-Barraza J, Wagner J, Muir A, Lau AN, et al. Netrin G1 promotes pancreatic tumorigenesis through cancer-associated fibroblast-driven nutritional support and immunosuppression. Cancer Discov 2021;11:446–79.
11. Elyada E, Bolisetty M, Laise P, Flynn WF, Courtois ET, Burkhart RA, et al. Cross-species single-cell analysis of pancreatic ductal adenocarcinoma reveals antigen-presenting cancer-associated fibroblasts. Cancer Discov 2019;9:1102–23.
12. Dominguez CX, Muller S, Keerthivasan S, Koeppen H, Hung J, Gierke S, et al. Single-cell RNA sequencing reveals stromal evolution into LRRC15(+) myofibroblasts as a determinant of patient response to cancer immunotherapy. Cancer Discov 2020;10:232–53.
13. Zhang Y, Lazarus J, Steele NG, Yan W, Lee HJ, Nwosu ZC, et al. Regulatory T-cell depletion alters the tumor microenvironment and accelerates pancreatic carcinogenesis. Cancer Discov 2020;10:422–39.
14. Feig C, Jones JO, Kraman M, Wells RJ, Deonarine A, Chan DS, et al. Targeting CXCL12 from FAP-expressing carcinoma-associated fibroblasts synergizes with anti-PD-L1 immunotherapy in pancreatic cancer. Proc Natl Acad Sci U S A 2013;110:20212–7.
15. Ozdemir BC, Pentcheva-Hoang T, Carstens JL, Zheng X, Wu CC, Simpson TR, et al. Depletion of carcinoma-associated fibroblasts and fibrosis induces immunosuppression and accelerates pancreas cancer with reduced survival. Cancer Cell 2014;25:719–34.
16. Provenzano PP, Cuevas C, Chang AE, Goel VK, Von Hoff DD, Hingorani SR. Enzymatic targeting of the stroma ablates physical barriers to treatment of pancreatic ductal adenocarcinoma. Cancer Cell 2012;21:418–29.
17. Jacobetz MA, Chan DS, Neesse A, Bapiro TE, Cook N, Frese KK, et al. Hyaluronan impairs vascular function and drug delivery in a mouse model of pancreatic cancer. Gut 2013;62:112–20.
18. Laklai H, Miroshnikova YA, Pickup MW, Collisson EA, Kim GE, Barrett AS, et al. Genotype tunes pancreatic ductal adenocarcinoma tissue tension to induce matricellular fibrosis and tumor progression. Nat Med 2016;22:497–505.
19. Olive KP, Jacobetz MA, Davidson CJ, Gopinathan A, McIntyre D, Honess D, et al. Inhibition of Hedgehog signaling enhances delivery of chemotherapy in a mouse model of pancreatic cancer. Science 2009;324:1457–61.
20. Steele NG, Biffi G, Kemp SB, Zhang Y, Drouillard D, Syu L, et al. Inhibition of hedgehog signaling alters fibroblast composition in pancreatic cancer. Clin Cancer Res 2021;27:2023–37.
21. Biasci D, Smoragiewicz M, Connell CM, Wang Z, Gao Y, Thaventhiran JED, et al. CXCR4 inhibition in human pancreatic and colorectal cancers induces an integrated immune response. Proc Natl Acad Sci U S A 2020;117:28960–70.
22. Van Cutsem E, Tempero MA, Sigal D, Oh DY, Fazio N, Macarulla T, et al. Randomized phase III trial of pegvorhyaluronidase alfa with Nab-paclitaxel plus gemcitabine for patients with hyaluronan-high metastatic pancreatic adenocarcinoma. J Clin Oncol 2020;38:3185–94.
23. Rhim AD, Oberstein PE, Thomas DH, Mirek ET, Palermo CF, Sastra SA, et al. Stromal elements act to restrain, rather than support, pancreatic ductal adenocarcinoma. Cancer Cell 2014;25:735–47.
24. Lee JJ, Perera RM, Wang H, Wu DC, Liu XS, Han S, et al. Stromal response to Hedgehog signaling restrains pancreatic cancer progression. Proc Natl Acad Sci U S A 2014;111:E3091–100.
25. Chen Y, Kim J, Yang S, Wang H, Wu CJ, Sugimoto H, et al. Type I collagen deletion in alphaSMA(+) myofibroblasts augments immune suppression and accelerates progression of pancreatic cancer. Cancer Cell 2021;39:548–65.
26. Jiang H, Torphy RJ, Steiger K, Hongo H, Ritchie AJ, Kriegsmann M, et al. Pancreatic ductal adenocarcinoma progression is restrained by stromal matrix. J Clin Invest 2020;130:4704–9.
27. Torphy RJ, Wang Z, True-Yasaki A, Volmar KE, Rashid N, Yeh B, et al. Stromal content is correlated with tissue site, contrast retention, and survival in pancreatic adenocarcinoma. JCO Precis Oncol 2018;2018:PO.17.00121.
28. Ohlund D, Handly-Santana A, Biffi G, Elyada E, Almeida AS, Ponz-Sarvise M, et al. Distinct populations of inflammatory fibroblasts and myofibroblasts in pancreatic cancer. J Exp Med 2017;214:579–96.
29. Hosein AN, Huang H, Wang Z, Parmar K, Du W, Huang J, et al. Cellular heterogeneity during mouse pancreatic ductal adenocarcinoma progression at single-cell resolution. JCI Insight 2019;5:e129212.
30. Neuzillet C, Tijeras-Raballand A, Ragulan C, Cros J, Patil Y, Martinet M, et al. Inter- and intra-tumoural heterogeneity in cancer-associated fibroblasts of human pancreatic ductal adenocarcinoma. J Pathol 2019;248:51–65.
31. Erkan M, Adler G, Apte MV, Bachem MG, Buchholz M, Detlefsen S, et al. StellaTUM: current consensus and discussion on pancreatic stellate cell research. Gut 2012;61:172–8.
32. Apte MV, Park S, Phillips PA, Santucci N, Goldstein D, Kumar RK, et al. Desmoplastic reaction in pancreatic cancer: role of pancreatic stellate cells. Pancreas 2004;29:179–87.
33. Sherman MH. Stellate cells in tissue repair, inflammation, and cancer. Annu Rev Cell Dev Biol 2018;34:333–55.
34. Hepatic stellate cell nomenclature. Hepatology 1996;23:193.
35. Mederacke I, Hsu CC, Troeger JS, Huebener P, Mu X, Dapito DH, et al. Fate tracing reveals hepatic stellate cells as dominant contributors to liver fibrosis independent of its aetiology. Nat Commun 2013;4:2823.
36. Yang L, Jung Y, Omenetti A, Witek RP, Choi S, Vandongen HM, et al. Fate-mapping evidence that hepatic stellate cells are epithelial progenitors in adult mouse livers. Stem Cells 2008;26:2104–13.
37. Riopel MM, Li J, Liu S, Leask A, Wang R. beta1 integrin-extracellular matrix interactions are essential for maintaining exocrine pancreas architecture and function. Lab Invest 2013;93:31–40.
38. Biffi G, Oni TE, Spielman B, Hao Y, Elyada E, Park Y, et al. IL1-induced JAK/STAT signaling is antagonized by TGFbeta to shape CAF heterogeneity in pancreatic ductal adenocarcinoma. Cancer Discov 2019;9:282–301.
39. Sherman MH, Yu RT, Engle DD, Ding N, Atkins AR, Tiriac H, et al. Vitamin D receptor-mediated stromal reprogramming suppresses pancreatitis and enhances pancreatic cancer therapy. Cell 2014;159:80–93.
40. He W, Barak Y, Hevener A, Olson P, Liao D, Le J, et al. Adipose-specific peroxisome proliferator-activated receptor gamma knockout causes insulin resistance in fat and liver but not in muscle. Proc Natl Acad Sci U S A 2003;100:15712–7.
41. Muzumdar MD, Tasic B, Miyamichi K, Li L, Luo L. A global double-fluorescent Cre reporter mouse. Genesis 2007;45:593–605.
42. Apte MV, Haber PS, Applegate TL, Norton ID, McCaughan GW, Korsten MA, et al. Periacinar stellate shaped cells in rat pancreas: identification, isolation, and culture. Gut 1998;43:128–33.
43. Bachem MG, Schneider E, Gross H, Weidenbach H, Schmid RM, Menke A, et al. Identification, culture, and characterization of pancreatic stellate cells in rats and humans. Gastroenterology 1998;115:421–32.
44. Iwaisako K, Jiang C, Zhang M, Cong M, Moore-Morris TJ, Park TJ, et al. Origin of myofibroblasts in the fibrotic liver in mice. Proc Natl Acad Sci U S A 2014;111:E3297–305.
45. Hingorani SR, Wang L, Multani AS, Combs C, Deramaudt TB, Hruban RH, et al. Trp53R172H and KrasG12D cooperate to promote chromosomal instability and widely metastatic pancreatic ductal adenocarcinoma in mice. Cancer Cell 2005;7:469–83.
46. Vennin C, Melenec P, Rouet R, Nobis M, Cazet AS, Murphy KJ, et al. CAF hierarchy driven by pancreatic cancer cell p53-status creates a pro-metastatic and chemoresistant environment via perlecan. Nat Commun 2019;10:3637.
47. Buch T, Heppner FL, Tertilt C, Heinen TJ, Kremer M, Wunderlich FT, et al. A Cre-inducible diphtheria toxin receptor mediates cell lineage ablation after toxin administration. Nat Methods 2005;2:419–26.
48. Chiou SH, Winters IP, Wang J, Naranjo S, Dudgeon C, Tamburini FB, et al. Pancreatic cancer modeling using retrograde viral vector delivery and in vivo CRISPR/Cas9-mediated somatic genome editing. Genes Dev 2015;29:1576–85.
49. Wang Y, Dorrell C, Naugler WE, Heskett M, Spellman P, Li B, et al. Long-term correction of diabetes in mice by in vivo reprogramming of pancreatic ducts. Mol Ther 2018;26:1327–42.

50. Rice AJ, Cortes E, Lachowski D, Cheung BCH, Karim SA, Morton JP, et al. Matrix stiffness induces epithelial-mesenchymal transition and promotes chemoresistance in pancreatic cancer cells. Oncogenesis 2017;6:e352.
51. Jiang H, Hegde S, Knolhoff BL, Zhu Y, Herndon JM, Meyer MA, et al. Targeting focal adhesion kinase renders pancreatic cancers responsive to checkpoint immunotherapy. Nat Med 2016;22:851–60.
52. Weissmueller S, Manchado E, Saborowski M, Morris JPIV, Wagenblast E, Davis CA, et al. Mutant p53 drives pancreatic cancer metastasis through cell-autonomous PDGF receptor beta signaling. Cell 2014;157:382–94.
53. Avery D, Govindaraju P, Jacob M, Todd L, Monslow J, Pure E. Extracellular matrix directs phenotypic heterogeneity of activated fibroblasts. Matrix Biol 2018;67:90–106.
54. Raz Y, Cohen N, Shani O, Bell RE, Novitskiy SV, Abramovitz L, et al. Bone marrow-derived fibroblasts are a functionally distinct stromal cell population in breast cancer. J Exp Med 2018;215:3075–93.
55. Garcia PE, Adoumie M, Kim EC, Zhang Y, Scales MK, El-Tawil YS, et al. Differential contribution of pancreatic fibroblast subsets to the pancreatic cancer stroma. Cell Mol Gastroenterol Hepatol 2020;10:581–99.
56. Manuyakorn A, Paulus R, Farrell J, Dawson NA, Tze S, Cheung-Lau G, et al. Cellular histone modification patterns predict prognosis and treatment response in resectable pancreatic adenocarcinoma: results from RTOG 9704. J Clin Oncol 2010;28:1358–65.
57. Auciello FR, Bulusu V, Oon C, Tait-Mulder J, Berry M, Bhattacharyya S, et al. A stromal lysolipid-autotaxin signaling axis promotes pancreatic tumor progression. Cancer Discov 2019;9:617–27.